Journal of Volcanology and Geothermal Research 441 (2023) 107878

Contents lists available at ScienceDirect

Journal of Volcanology and Geothermal Research

journal homepage: www.journals.elsevier.com/journal-of-volcanology-and-geothermal-research

# Lava – substrate interaction: Constraints on flow emplacement and basal sintering, Lebuj rhyolitic flow, Tokaj Mountains, Carpathian-Pannonian region

János Szepesi [a,b,*], Alessandro Vona [c], István János Kovács [d], Krisztián Fintor [e], Kata Molnár [a], Alex Scarani [c], Guido Giordano [c,f], Réka Lukács [b,g,h]

[a] Isotope Climatology and Environmental Research Centre (ICER), Institute for Nuclear Research, Debrecen (ELKH), Bem tér 18/c, 4026 Debrecen, Hungary
[b] MTA-ELTE Volcanology Research Group, Eötvös Loránd Research Network (ELKH), Pázmány P. sétány 1/C, 1117 Budapest, Hungary
[c] Dipartimento di Scienze, Università degli Studi Roma Tre, L.go San Leonardo Murialdo 1, 00146 Roma, Italy
[d] Institute of Earth Physics and Space Science, (ELKH) Csatkai E. u. 6-8, 9400 Sopron, Hungary
[e] Vulcano Petrology and Geochemistry Research Group, Department of Mineralogy, Geochemistry and Petrology, University of Szeged, Egyetem utca 2, 6722 Szeged, Hungary
[f] Instituto di Geologia Ambientale e Geoingegneria, CNR, Montelibretti, Italy
[g] Institute for Geological and Geochemical Research, Research Centre for Astronomy and Earth Sciences, (ELKH), Budaörsi út 45, 1112 Budapest, Hungary
[h] CSFK, MTA Centre of Excellence, Konkoly Thege Miklós út 15-17, Budapest H-1121, Hungary

ARTICLE INFO

*Keywords:*
Rhyolite
Obsidian-perlite
Hydration
Basal contact
Substrate
Lithification

ABSTRACT

The surface extrusion of rhyolite lava is linked with a complex edifice morphology and texturally diverse internal structure. The rarely exposed basal flow/dome zones provide a textural record of the mechanical and thermal stress between the overlying lava and existing topography. The Lebuj flow (Tokaj Mountains, Hungary) developed in a Miocene caldera setting, where the erosion exposed its basal zone, including various textures due to the lava substrate interaction. The flow margin is contacted with underlying volcaniclastics along a steeply inclined (50–75°) plane. The lithology describes a complex ductile-brittle transition in the flow and lithification process in the substrate. The relict obsidian grains (marekanite, 0.1% $H_2O$) in the perlite (2–3% $H_2O$) are proof of an incomplete hydration process below the glass transition temperature. The dynamic loading of the lava caused irregular fragmentation developing a brittle basal shear zone with lens-like glass deformation. The substrate has suffered *syn*-emplacement lithification and the primary glass structure is completely re-crystallized. FTIR and Raman measurements identified low-temperature phyllosilicate minerals and $SiO_2$ polymorphs, which caused additional porosity loss and densification. Using cooling time-temperature-porosity information given by this reconstruction, we suggest parallel-acting processes at elevated (groundmass crystallization-devitrification) and lower temperature (hydration-secondary mineralization) range. These define a relative timescale for the textural development in the lithologically heterogeneous contact zone.

## 1. Introduction

Effusive silicic volcanism produces a wide range of textures which develop by cooling (microcrystalline and glassy) and autoclastic fragmentation (carapace and basal breccias) processes of the flow/dome complexes (Manley, 1996; Manley and Fink, 1987; Castro et al., 2002; Shields et al., 2016; Szepesi et al., 2018). In recent years, particular attention has been paid to several processes during the emplacement, especially hydration (Bindeman and Lowenstern, 2016; Seligman et al., 2016), groundmass crystallization (Rowe et al., 2012; Breitkreuz, 2013; Ellis et al., 2015) and spherulite formation (Befus et al., 2015; Gardner et al., 2012; Watkins et al., 2009; Bustos et al., 2020). The exposure of basal shear zones depends on the age and erosion level but occurs less frequently than the talus cover (McLean et al., 2016). Such flow base

* Corresponding author at: Isotope Climatology and Environmental Research Centre (ICER), Institute for Nuclear Research, Debrecen (ELKH), Bem tér 18/c, 4026 Debrecen, Hungary.
*E-mail addresses:* szepeja@gmail.com (J. Szepesi), kovacs.istvan.janos@epss.hu (I.J. Kovács), molnar.kata@atomki.hu (K. Molnár), alex.scarani@uniroma3.it (A. Scarani), guido.giordano@uniroma3.it (G. Giordano), lukacs.reka@csfk.org (R. Lukács).

https://doi.org/10.1016/j.jvolgeores.2023.107878
Received 6 April 2023; Received in revised form 29 July 2023; Accepted 1 August 2023
Available online 5 August 2023

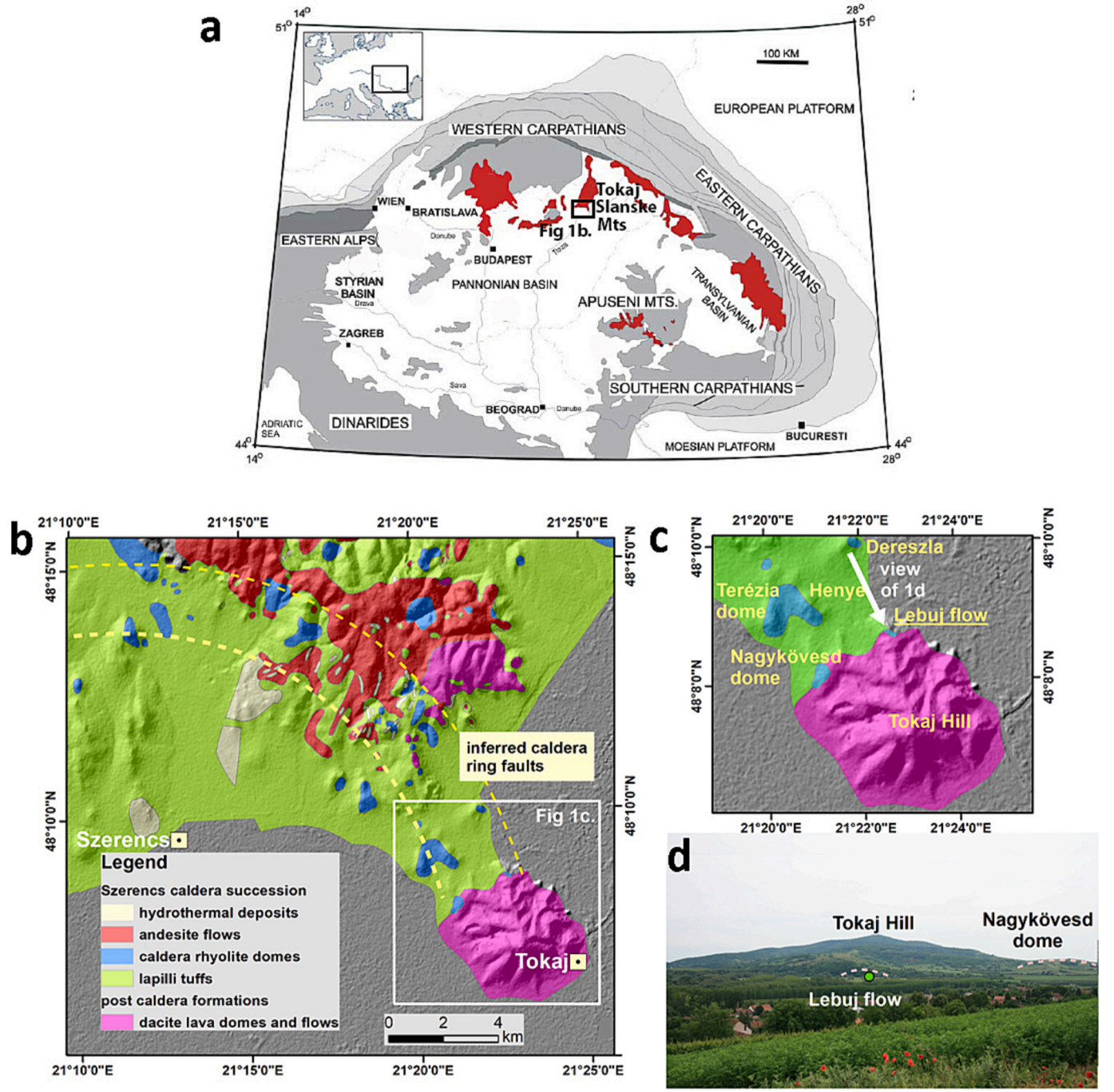


**Fig. 1.** (a) Geological sketch of Carpathian–Pannonian region showing the position of the Tokaj-Slanske Mts and Szerencs caldera, red colour indicates Miocene calc-alkaline volcanic rock (based on Seghedi et al., 2004). (b) Geological map of the north-eastern segment of the Szerencs caldera succession. (c) Close-up of the area near the Lebuj rhyolitic flow at the eastern caldera margin. (d) Field photography of the study area with the location of the Lebuj flow (boundary dashed) and the post-caldera dacite volcano of Tokaj Nagyhegy (Tokaj Hill, the picture was taken from the north, top of Dereszla rhyolite dome). (For interpretation of the references to colour in this figure legend, the reader is referred to the web version of this article.)

usually passes over the ductile-brittle transition and has undergone progressive deformation (Bull and McPhie, 2007). Thick flows and domes can impose mechanical and thermal stress on the underlying substrate. This can be directly studied in eroded edifices with exposed contacts where sediment deformation and peperite formation (soft substrate) or autoclastic fragmentation (hard/mixed substrate) occurred. A hard substrate may cause the propagation of basal shear zone with the development of monomictic breccias, e.g., Minyon Falls, (Smith, 1996); Calico Hills Formation, (Sweetkind and Bova, 2015). Additional clast rotation and ductile flattening may result in secondary foliation and stretched autoclast (lens-like) formation (Bull and McPhie, 2007). In direct contact, the lavas also have an effect on the substrate. Mechanical and thermal erosion occur in lava tubes and channels (Fagents and Greeley, 2001; Williams et al., 2004; Gallant et al., 2020), where the substrate may be incorporated or assimilated and travels toward. The unconsolidated substrate material may be subject to *syn*-eruptive densification and deformation at a given temperature and pressure (flow base, conduit). This is even more true in presence of circulating meteoric water which allow limited low temperature hydrothermal activity to occur with precipitation of new mineral phases

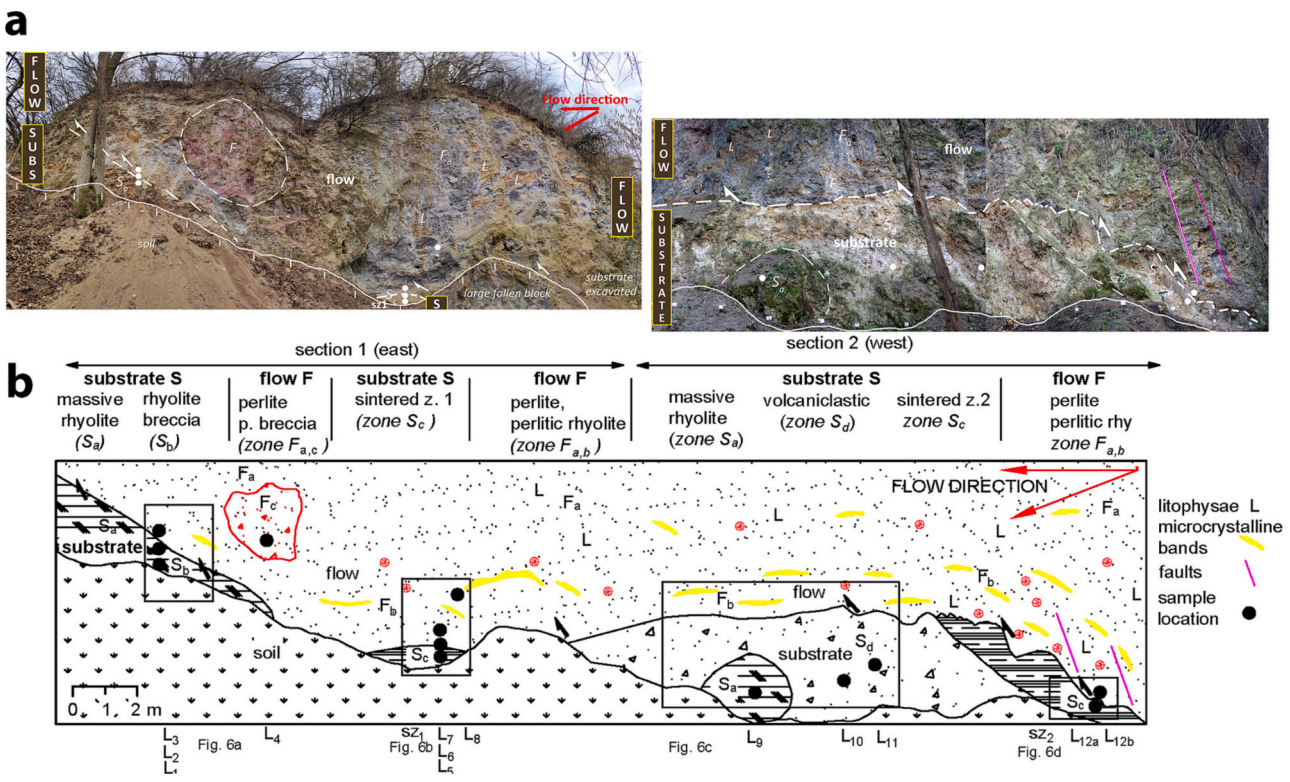


**Fig. 2.** Outcrop photographs (a) and lithological sketch (b) of the key section. (a) The photographs are looking to the south and the sectioning was done with a meter line spacing. The upper rhyolitic lava flow (dark grey) and the mixed substrate units (yellow) are divided by a dashed line. The substrate section exposes two major sintering zones (SZ $_1$, SZ$_2$; see Fig. 6c,d). Individual textural elements such as lithophysae (L), microcrystalline bands (yellow) and shear planes (purple lines) are highlighted in the figure. (b) Lithofacies sketch of the outcrop (dots) and names ($L_1$-$L_{12b}$) are marked together with the above-mentioned features. Black boxes are the position of the images from Fig. 6. (For interpretation of the references to colour in this figure legend, the reader is referred to the web version of this article.)

(fluid accelerated densification, Ryan et al., 2020).

Here, we focus on a crystal-poor, glassy Miocene rhyolitic lava flow base from the Szerencs Caldera (Carpathian-Pannonian Region, Fig. 1), where long-lasting erosion has exposed a basal shear zone and sintered volcaniclastic substrate. Our study presents field-based textural descriptions of the lava-mixed substrate contact. Additionally, FTIR and Raman spectrometry quantify glass water content and identify mineralogy of the microcrystalline textures. Based on these, we describe and interpret (1) the groundmass crystallization-hydration processes of the silicic lava flow, including ductile-brittle transition in the glassy domain and (2) the densification and mineralization process of the underlying volcaniclastic substrate. Finally, we define a thermal model and relative timescale for lava flow cooling and the described substrate lithification process.

## 2. Textural framework for identification processes at silicic lava flow bases

The formation of a silicic dome/flow complex represents a coherent core and (auto) clastic, fragmented (talus) components (Ball et al., 2015). Formation of the described widespread textures beneath silicic flows (e.g. Smith, 1996; McLean et al., 2016) depends on the volume loading and heating of the cooling lava on the variable consolidated substrate. Inside the coherent core, the microcrystalline features formed above glass transition temperatures ($T_g$), while the glassy facies (dense and autoclastic) develop cooling below $T_g$ (Giordano et al., 2005; Breitkreuz, 2013; Befus et al., 2015). The spherulites and fine grained groundmass (felsite) are interpreted as groundmass crystallization product formed above $T_g$ as suggested by Ellis et al. (2015). The devitrification term used for microcrystalline features generally forms generally below $T_g$. The primary glass (obsidian) may suffer secondary hydration (also below $T_g$) and perlite formation can continue to ambient temperature (Anovitz et al., 2008). The relict obsidian nodules in perlite are named marekanite in the early hydration studies (Friedman and Smith, 1958) from type locality Siberia (Russia). Cooling of the flow base can lead to lava behavior passing through the ductile brittle transition (autoclastic fragmentation, Smith, 1996), where the elongated lenses are referred as flame-like textures (Bull and McPhie, 2007). The lava flow loading on the substrate is a thermo-mechanical process (Gallant et al., 2020) considered a trigger for fluidization on fluid-saturated sediments allowing deformation structures and peperites formation (McLean et al., 2016). In contrast, the heat retention of the flows on a relatively "dry" substrate caused agglutination (sintering) and porosity loss. In this study, the term sintering is used in a broader sense which followed by precipitation of secondary mineral phases in the late stages of lithification (fluid accelerated densification, Ryan et al., 2020) resulting in a dense composite.

## 3. Geological settings

The study area is located on the eastern flank of the Szerencs silicic caldera, which is a structure at the southern end of the Tokaj-Slanske Mts. (TSM, Fig. 1a) in the Carpathian-Pannonian Region (Hungary). The TSM evolved during the middle-late Miocene (15–9.6 Ma, Pécskay et al., 1987, Pécskay et al., 2006) and exhibits preserved volumes of lavas and volcanoclastites estimated to be approximately 600 km$^3$ (Karátson and Timár, 2005). The stratigraphy contains products of the contemporaneous andesitic-rhyolitic explosive-effusive eruptions between ca. 15–10 Ma (Pécskay et al., 1987; Kiss et al., 2010). The volcanic landforms include silicic caldera structures with lava domes, andesitic-dacitic composite volcanoes and subvolcanic bodies (Gyarmati, 1977; Zelenka et al., 2012; Szepesi et al., 2019). The Szerencs

caldera structure was identified by the Celebration (CEL-4) deep seismic profile (Hegedűs et al., 2002) and magnetic gradient map (Zelenka et al., 2012), outlining a buried ring structure with approximately 25 km in diameter (Fig. 1b).

The eruptive stratigraphy related to the formation of Szerencs caldera was previously dated by conventional K/Ar geochronology (Pécskay et al., 1987; Pécskay and Molnár, 2002). Based on borehole stratigraphy, the major lithologies comprise (Zelenka, 1964; Szepesi et al., 2018): a large thickness (10-150 m) of rhyolitic pyroclastic rock horizons (5 major variably altered lapilli tuff units) with high silica rhyolites (12.2–11.3 ± 0.5 Ma), late stage effusive andesites (11.5 ± 0.5 Ma), dacites (10.7 ± 0.5 Ma) and hydrothermal deposits (alunite K/Ar age: 11.7–10.9 ± 0.3 Ma).

The pyroclastic deposits accumulated under submarine and subaerial conditions (Zelenka, 1964; Zelenka et al., 2012). The subaerial deposits form a mixed substrate below the studied lava flow. The lapilli tuff deposition was simultaneous with lacustrine sedimentation and caldera hydrothermal activity (Molnár et al., 1999; Pécskay and Molnár, 2002), including acid-sulphate steam heated zones (180–200 °C) with strong silicification and alunite-kaolinite alteration halos. The intermediate effusive volcanism was connected to the peripheral faults of the caldera. Based on fieldwork and borehole logs, high silica lava domes (74–77 wt % $SiO_2$) developed during at least two major phases (Zelenka, 1964; Szepesi et al., 2018). The Lebuj flow is connected to a dome field developed on the eastern flank of the Szerencs caldera structure (Fig. 1c), which comprises six small-volume (<0.02 $km^3$) units (ca. 11.2 Ma) exposed as variably eroded edifices. Some of these are covered by the youngest post-caldera dacitic lavas (Fig. 1d), which postdate the hydrothermal activity.

## 4. Methods

Samples were collected from each lithological unit (Fig. 2) with continuous (15 cm) textural sampling at the lava – substrate boundaries (sintering zones Fig. 2). The exact topographic and lithological positions were recorded for each sample. Porosity and densification scale (>30%-low, 10–30%-moderate, <10%-high) estimated by image processing in hand specimen and thin section scale. Double-polished thick sections (100 μm) were used to determine the water content of different textures by a Bruker Vertex 70 spectrometer and a Bruker Hyperion 1000 infrared microscope unit at the Institute of Forensic Science and Research (Budapest, Hungary) equipped with a broadband MCT detector with an aperture size of 100 μm × 100 μm. The applied nominal spectral resolution was 4 $cm^{-1}$ and the absorbance was recorded in the wavenumber range between 400 and 6000 $cm^{-1}$.

Concentrations of $H_2O$ species can be measured in Lebuj glasses using absorbances at wavenumbers 3570 $cm^{-1}$ for total water ($H_2O_{tot}$), 4500 $cm^{-1}$ for $OH^-$ (Mandeville et al., 2002), and 1630 $cm^{-1}$ and 5230 $cm^{-1}$ for $H_2O$ molecular. All absorbances measured are relative to a linear baseline. The sum of these species represents the total water content ($H_2O_{tot}$) of the sample, which is converted to concentrations using the Beer-Lambert law (Stolper, 1982):

$$C = \frac{M_W * A}{\varepsilon * \rho * d} * f$$

where C is the concentration of the $H_2O_{tot}$ in wt%, MW is the molecular weight of the volatile species in g $mol^{-1}$, A is absorbance, d is thickness in cm, ρ is glass density in kg $m^{-3}$, ε is the molar absorptivity coefficient in L $cm^{-1}$ $mol^{-1}$, and f is a dimensionless conversion factor ($10^2$ for $H_2O$).

Raman mapping was performed at the Department of Mineralogy, Geochemistry and Petrology (University of Szeged, Hungary) for the mineralogical analysis of microcrystalline textural variations using a Thermo Scientific DXR Raman microscope with a 532.2 nm wavelength, 5 mW Nd-YAG solid-state diode laser. The spectra were collected using a Peltier cooled CCD detector. The spectral resolution was 4 $cm^{-1}$ in the wavenumber range of 120–1850 $cm^{-1}$. The 5 × 1 mm maps were obtained by recording 2121 spectra. The RRUFF (Lafuente et al., 2015) international database was used to identify the Raman bands for each mineral. Whole-rock major element chemical compositions of the samples were determined by inductively coupled plasma optical emission spectrometry (JY Ultima 2C) at Laboratory of Hungarian Mining and

**Table 1**
Description of Lebuj flow and mixed substrate units, including textural and mineralogical properties.

a, upper flow unit

| *descriptive name* | *texture* | *porosity* | *additional features* |
|---|---|---|---|
| massive perlite (zone $F_a$) | dense, non-vesicular, banded glass with curvy planar, onion-like foliation and obsidian (marekanite) nodules | <5%, generally dense glass, curvy planar and longitudinal hydration cracking | decimeter sized lithophysae, hydration rim of the obsidian cores, Fe oxide microlites |
| perlitic rhyolite (zone $F_b$) | discontinuous, elongated devitrified bands, spheroidal microcrystalline masses, micro to crypto crystalline groundmass, strong planar alignment | <10%, variable filled (tridymite) cavities (mm-cm) | large lithophysae (dm) with concentric crystallized rims, micro- and meso scale folding |
| perlite breccia (zone $F_c$) | matrix poor, clast supported monomictic (cm-dm) breccia, frequent clast rotation and fiamme-like flattening | elevated matrix porosity: 10–40%, minor pore collapse or deformation, perlitic clast fracturing | rare massive rhyolite lithics, sharp transition between coherent and autoclastic part |

b, hard substrate

| *descriptive name* | *texture* | *porosity* | *additional features* |
|---|---|---|---|
| massive rhyolite (zone $S_a$) | yellowish - grey – pink microcrystalline groundmass with darker crypto crystalline bands | <5%, rounded cavities (no shear), tridymite filling, minor clays | frequent spherulites |
| rhyolite breccia (zone $S_b$) | matrix poor, clast supported monomictic (mm-cm) breccia, minor clast rotation | 5–15% fragmentation induced porosity, densification rank: moderate-to high | imperfect alignment, jig saw fit textures |

c, variable consolidated volcaniclastic substrate

| *descriptive name* | *texture* | *porosity (estimated densification rank)* | *additional features* |
|---|---|---|---|
| strongly densified volcaniclastics (zone $S_c$) | yellowish white, pervasively devitrified micro to cryptocrystalline texture, scattered spherulites | no connected porosity (<5%), tridymite, cristobalite filled cavities densification rank: high | sharp transition with lava; concentric re-crystallized structures (accretionary lapilli?) |
| moderately densified lithic-rich lapilli tuff (zone $S_d$) | altered, oxidized, matrix to clast supported, unsorted lapilli tuff, angular to rounded, lithics: microcrystalline rhyolites (0.5 -15 cm) | partially filled (tridymite, cristobalite) pore spaces (5–10%) in the altered, re-crystallized matrix densification rank: moderate to high | large angular lithics, rounded rhyolite lapilli, partly re-crystallized glassy concretions |

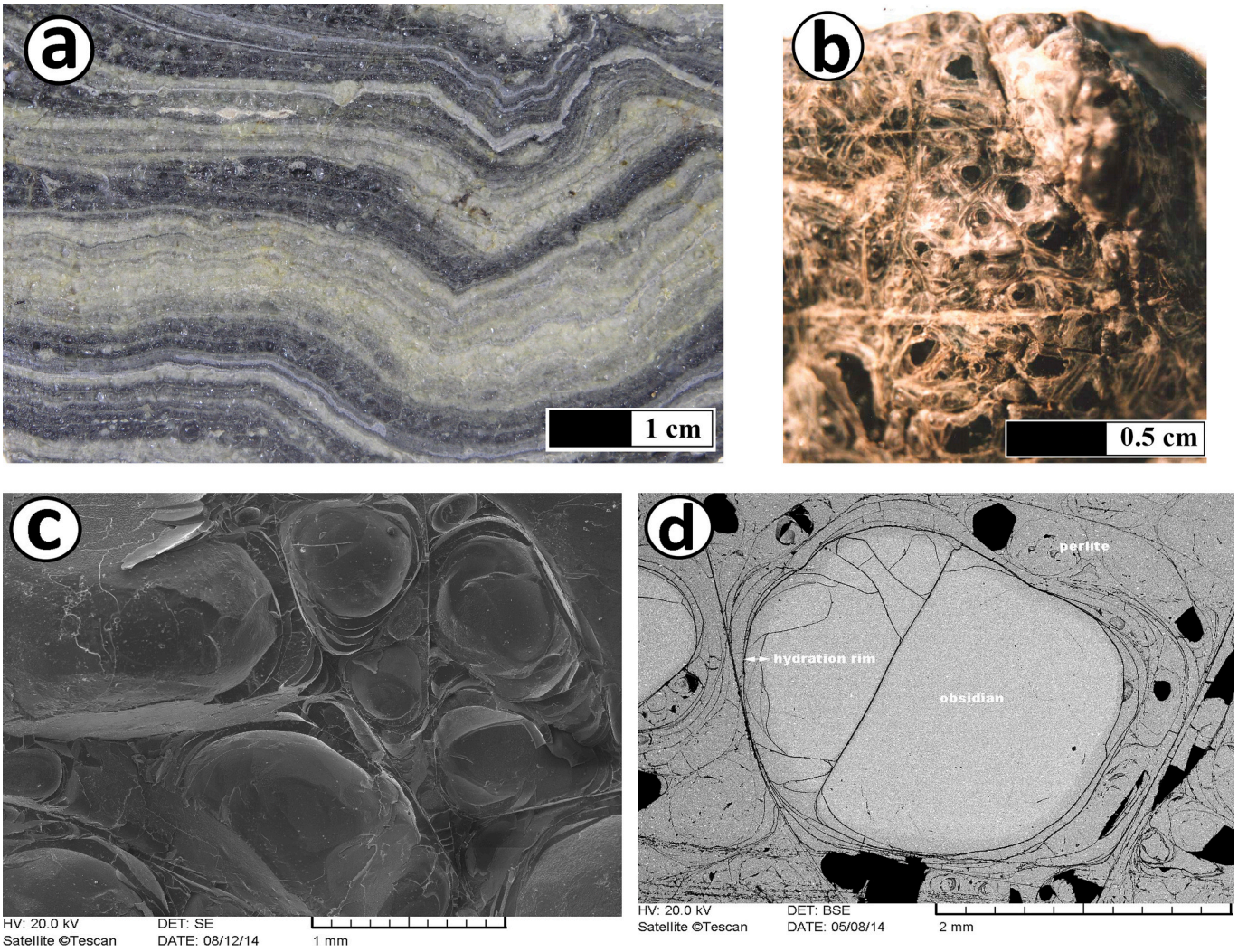


**Fig. 3.** Macro photographs (a, b), secondary electron (SE, c) and backscatter electron (BSE, d) images of the coherent perlite (zone $F_a$, sampling point $L_8$, see Fig. 2 and Fig. 6b). (a) Banded texture of the perlite. (b) Banded perlite with nested obsidian "marekanite" grains and longitudinal cracks. (c) Onion-like foliation around the "marekanite". (d) Obsidian marekanite (light grey) and hydrated perlite (dark grey) with onion-like foliation, longitudinal cracks, and hydration front at the rim of the marekanite.

Geological Service (Budapest, Hungary), the $H_2O^+$ and $H_2O^-$ content were measured by gravimetry. Scanning electron microscopic textural analyses were performed at the Department of Petrology and Geochemistry, Eötvös Loránd University (Budapest, Hungary), using an AMRAY 1830 type SEM with a 20 kV accelerating voltage backscattered electron (BSE) detector.

## 5. Results

### 5.1. Lithofacies architecture

The Lebuj flow erupted on the mixed, variable consolidated substrate and is exposed in the 150 m long road cut (between Tokaj and Bodrogkeresztúr, Fig. 1) The outcrop height varies between 1 and 10 m. The key section (Fig. 2) where the substrate exposed is only 50 m (eastern part), represents the basal contact between high silica lava and the volcaniclastic materials. The rest of the cut reveals only the lava flow core. The lithologies were described (Table 1) using a flow/dome textural stratigraphy approach developed for Telkibánya Lava Dome Field (Szepesi et al., 2019) based on international analogues (e.g. Manley and Fink, 1987). The autoclastic glassy carapace has been completely removed by erosion, revealing the dense glassy and microcrystalline core material.

The main units comprise (1) a rhyolitic lava flow (flow; Fig. 2) and (2) the underlying substrate unit (substrate; Fig. 2). The contact of the rhyolite flow and the underlying mixed volcanic substrate is an undulating and steeply inclined (50–75°) surface plane. At the western side, subvertical foliation and shear planes developed (Fig. 2) parallel to the flow margin. On the eastern side, the volcaniclastic material is absent, and the flow is in direct contact with the older dome material.

### 5.2. The Lebuj flow unit

The Lebuj flow sequence comprises of a coherent core and subordinate clastic components and includes three distinct but intergradational lithofacies (zone $F_{a-c}$). The coherent part consists of a massive (dense) perlite (zone $F_a$) and glass-microcrystalline transition (perlitic rhyolite zone $F_b$; Fig. 2) with 2–10 m thickness. The texture shows well-defined flow banding parallel with the contact, and comprises alternating darker (glassy) and lighter (microcrystalline) bands of mm-cm thickness (Fig. 3a). Large decimeter-size, isolated lithophysae appear at the upper part of the outcrop (Fig. 2a).

The hydrated glass contains nested obsidian grains (0.5-1 cm; Fig. 3b) which is traditionally called "marekanite" (Friedman and Smith,

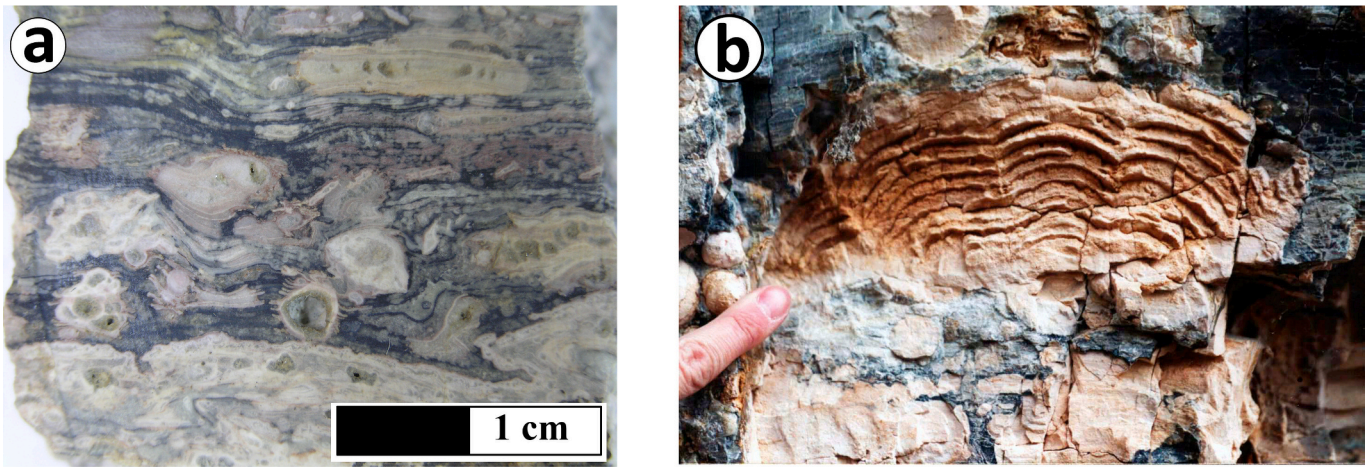


**Fig. 4.** Outcrop and macro photographs of the microcrystalline-glass transition (zone $F_b$, sampling point $L_{6–7}$, see Fig. 2). (a) Glassy (dark) and micro-crystalline domains (light colored) with deflected flow bands and restricted lithophysae opening, the photographic view is parallel with contact shear planes. (b) Large >10 cm lithophysae with concentric crystallization rims.

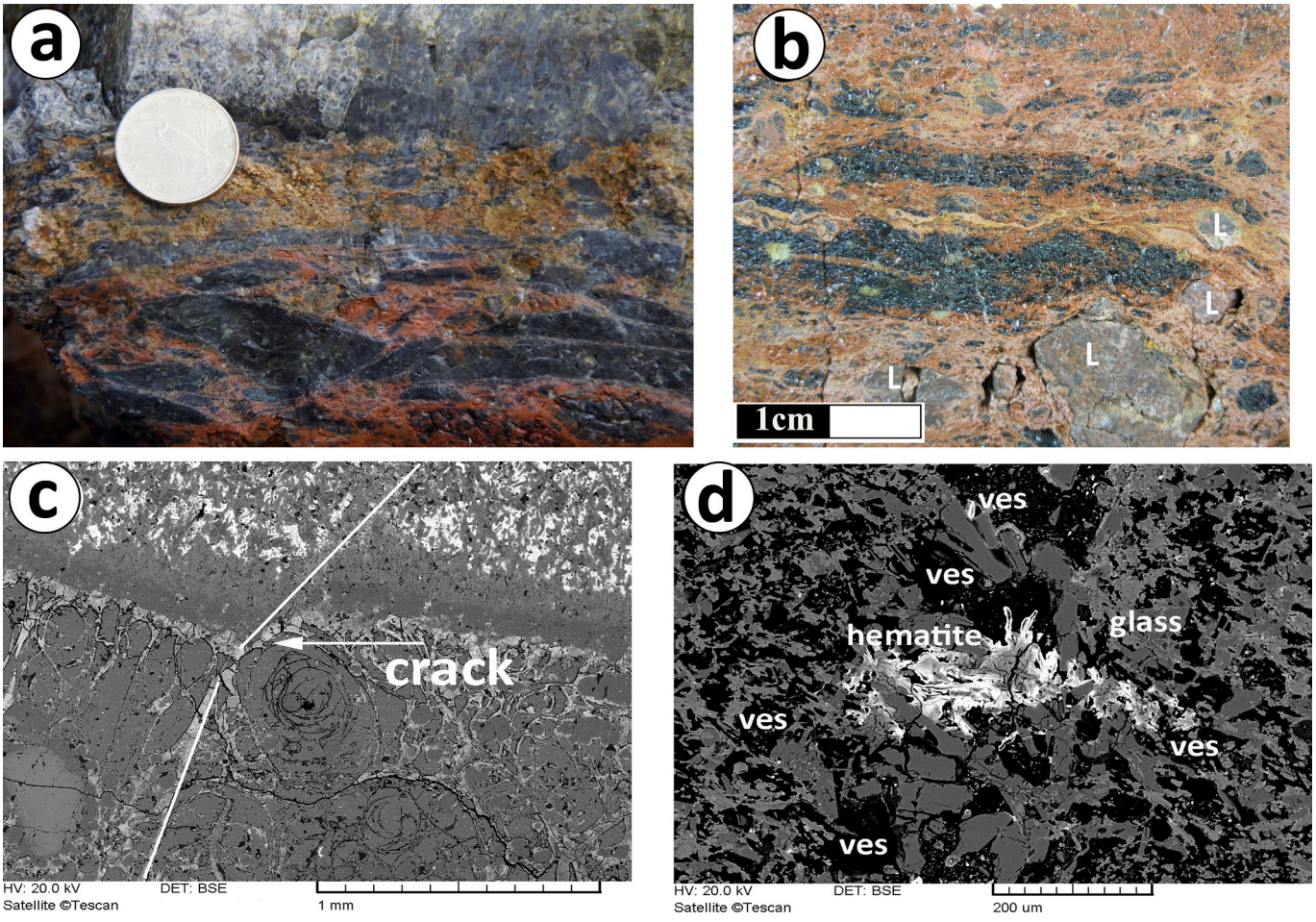


**Fig. 5.** Macro photographs and BSE images of the ductile-brittle transition zone (zone $F_c$, sampling point $L_4$, see Fig. 2) (a) Coherent (dark perlite)-fragmental (breccia) transition in the basal shear zone with clast rotation and flattening. (b) Lens-like texture with elongated glassy domains in the red oxidated matrix, the incorporated microcrystalline (rhyolite) lithics (L) caused clast deformation. (c) BSE image of the black perlite clast and the matrix contact with onion skin-like foliation in the perlite and vesicular character and hematite (bright) coloring in the matrix coatings. (d) Close up on the matrix having elevated porosity (black, ves.) and hematite content. (For interpretation of the references to colour in this figure legend, the reader is referred to the web version of this article.)

1958). The obsidian nodules have curvy planar surfaces, and the nesting perlite forms onion-like foliation around the cores (Fig. 3b, c). The perlitic fracturing is defined at macro (cm) and micro-scale (Fig. 3b, c, d). The perlitic bead diameters vary from 0.2 to 1 cm, bounded by curved and longitudinal cracks (Fig. 3b, d). The marekanite (obsidian modules) has lighter grey colour on the BSE image (Fig. 3d) compared to

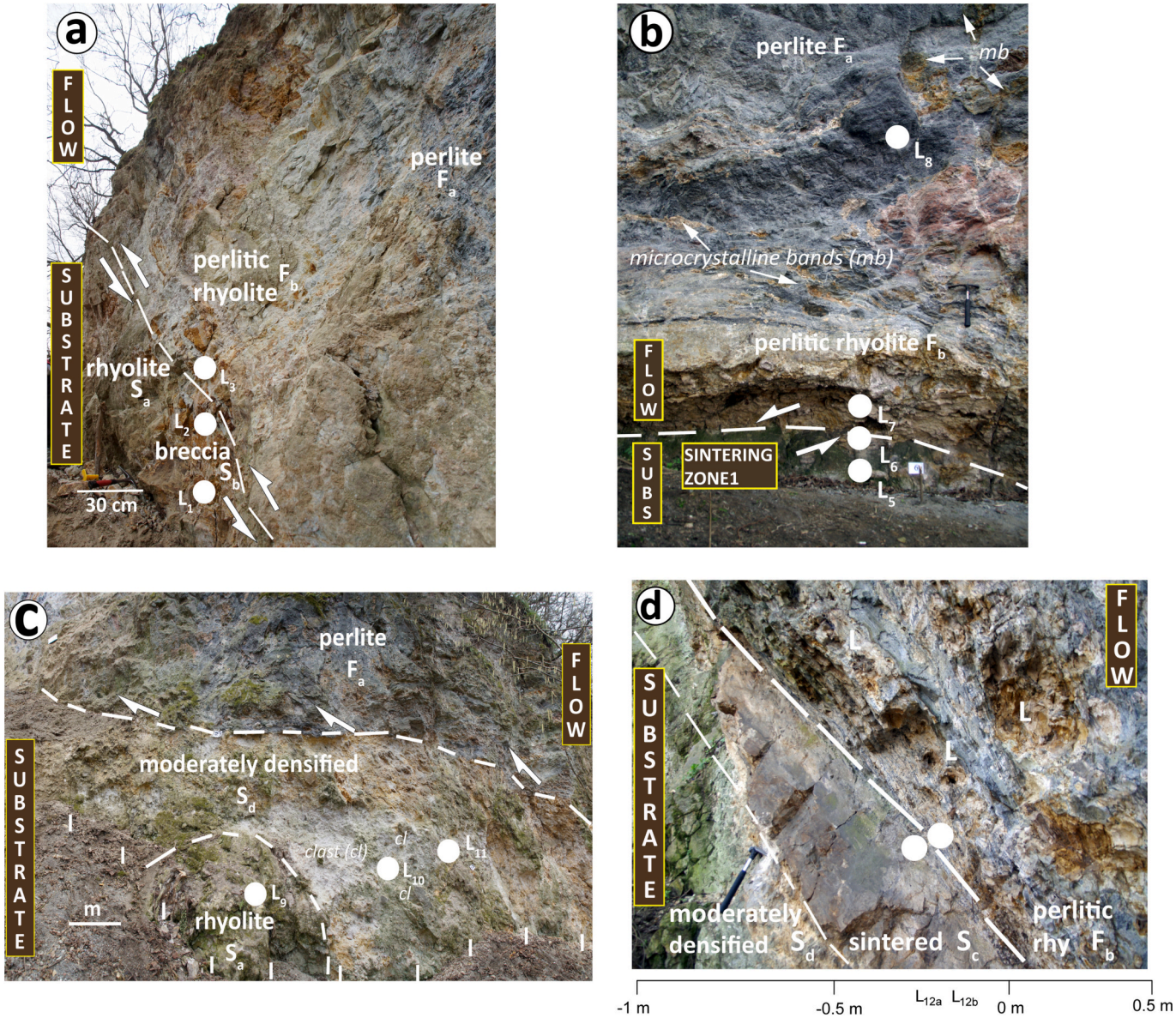


**Fig. 6.** Outcrop photographs of different types of contact between the flow and the substrate (see Fig. 2 for the stratigraphic positions). (a) Massive rhyolite (hard substrate) and flow contact (section 1, east). (b) Sintering zone 1: strongly densified volcanoclastite ($S_c$) and the flow (section 1, east). (c) Mixed substrate with massive rhyolite ($S_a$) and moderately densified volcanoclastite ($S_d$) with the upper flow unit (section 2 (west). (d) Sintering zone 2 ($S_c$, section 2, west), defining the boundary between the flow and the substrate.

the hydrated glass (perlite). The width of the hydration rim is between 0.1 and 0.3 cm. The hydrational cracking cut through the obsidian nodules.

Toward the contact, a glass-microcrystalline transition zone (zone $F_b$; Fig. 4) with a thickness of 1–3 m was identified (see Fig. 2). The microcrystalline material appears first as dense, elongated bands in the glass and stretched by flow foliation dominated by the glass (above the 1st sintering zone; Fig. 2). In a slightly deeper position (above the 2nd sintering zone; Fig. 2, 4b) these yellowish colored microcrystalline domains dominate the texture. Lithophysae opening are usually deflected flow bands (Fig. 4a) and defining *meso*-scale folding. The larger lithophysae (3–10 cm) generations developed with concentric crystallized rims most frequently (Fig. 4a,b) above the contact. The spheroidal masses (cm, spheruloid, Breitkreuz, 2013), spherulites (mm) with micro- to crypto-crystalline groundmass are also common in the texture and sometimes overprinted the foliation.

The subordinate, clastic, reddish colored flow border zone (zone $F_c$; Fig. 5) was identified as an isolated, discontinuous lithological domain wedging between the massive core and the substrate. The clast-supported perlite breccia comprised of dark perlitic clasts (up to dm), are embedded in a co-genetic, red-colored matrix (40–70%) composed of fine glass shards and a micro-vesicular groundmass. The clasts are angular to subangular (mm to dm), showing typical onion-like perlitic fracturing (Fig. 5c). The clast rotation and alignment are well defined. The larger clasts suffered lens-like flattening and are elongated in the flow direction with relatively high length/width ratios (over 5:1, Fig. 5b). Lithic rhyolite fragments of the older dome bedrock (~cm) are sometimes incorporated. The relatively more resistant lithic fragments deformed the shear and flattening planes of the flow texture (Fig. 5a, b). The black glass shows fracturing along micro-cracks (Fig. 5c). The porosity is elevated only in the breccia matrix domains (Fig. 5c). The micro-vesicular matrix shows irregularly shaped pores with minor collapse and deformation (Fig. 5d). The reddish coloring is caused by hematite (BSE, white patches, Fig. 5c, d).

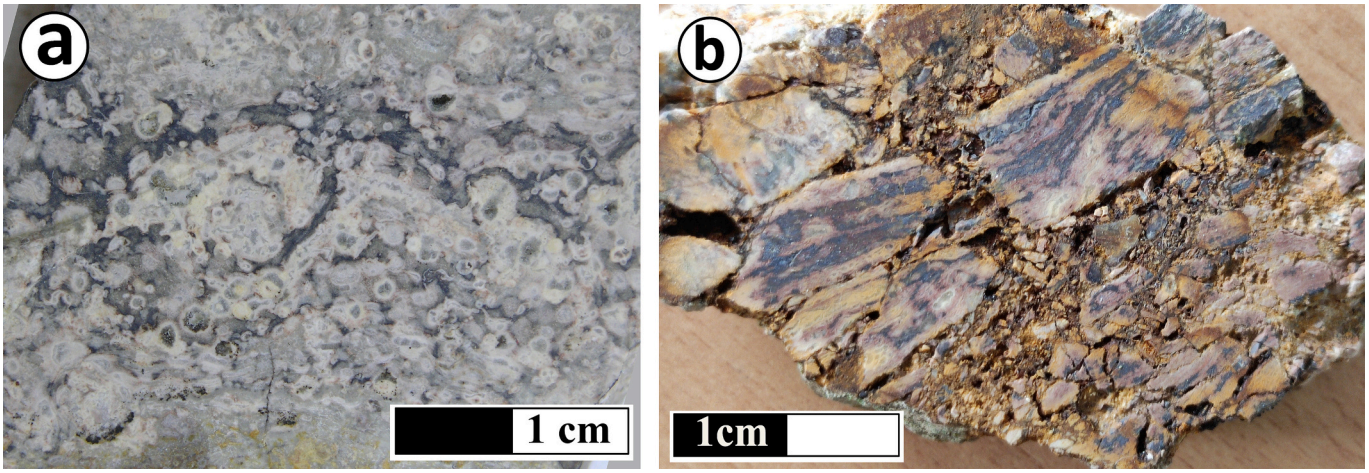


**Fig. 7.** Macro photographs of the hard substrate rhyolite (zone $S_a$, sampling point $L_{1-2}$). (a) Grey-pink textural domains with different crystallinity. (b) Yellowish-brown rhyolite breccia ($S_b$) from the contact with the jig saw fit texture and elevated porosity (5–15%). (For interpretation of the references to colour in this figure legend, the reader is referred to the web version of this article.)

### 5.3. Substrate lithology

At the eastern side of the road cut (key section, Fig. 2), the lava flow made contact with the mixed substrate. The steep, inclined surface contact zone is visible only along the plane of the wall (but seems more horizontal from the front). The substrate comprises four other lithofacies ($S_{a-d}$): an older dome unit (massive microcrystalline rhyolite; zone $S_a$) and rhyolite breccia (zone $S_b$, Fig. 6). The volcaniclastic substrate wedged between the older dome and the lava flow, which includes the variable consolidated volcaniclastics (zone $S_{cd}$). The massive rhyolite (zone $S_a$) cropped out in two sampling points (Fig. 2, 6a, c). The direct contact of the massive rhyolite substrate with an overlying lava flow can be observed only on the most eastern side (Fig. 6a), where the volcaniclastic material is absent.

The rhyolite has a massive texture with yellowish- grey-pink colored and rounded lithophysae (<1 cm). Cooling fractures are frequent, giving permeability. The microcrystalline groundmass shows crystallinity differences between the irregular dark and light bands (Fig. 7a). At the contact, locally a clast-supported (0.1–3 cm), monomictic rhyolite breccia is developed ($S_b$, Fig. 7b). The clast shapes are angular to subrounded. The high porosity (5–15%) is highlighted by fragmentation, clast rotation and imperfect alignment (jig saw fit) parallel to the extrusion direction.

The upper part of the substrate is a dense, variable sintered, volcaniclastic material (zone $S_c$). The yellow-white, strongly densified tuff layer is discontinuous, crops out in two major points (sintered tuff 1&2 Figs. 2, 6 b, d) The thickness is 30–70 cm and developed directly below the basal part of the flow with a sharp transition (Fig. 8a, b). The texture is dense without connected porosity (<5%, high densification rank) and dominated by fine-grained devitrification domains (grey-white), enclosing irregular or spherical masses (white, Fig. 8a, b). One of these domains revealed a relict accretionary lapilli structure with the characteristic multiple rim zonation (Fig. 8c). Undeformed substrate rhyolite clasts ($S_a$) are observable. The groundmass underwent a pervasive recrystallization and devitrification with production of micro-crystalline texture, including small spherulites. The BSE image (Fig. 8d) shows visible contrast and mineralogical differences between the foliated flow and massive sintered material.

Moving away from the contact, a moderately densified zone (zone $S_d$) developed (Fig. 2) with a decreasing compaction intensity (moderate to high densification rank). The thickness of crumbly, unconsolidated, volcaniclastic material varied between 1 and 5 m (Figs. 6c, 9a). Rounded lithics (0.5–15 cm Ø; Fig. 9b) are incorporated (L, Fig. 9c). The matrix comprises yellowish-white, variable altered glass with slightly elevated porosity (10–15%) comparing to $S_c$. The primary vitroclastic texture is obscured by intensive secondary mineralization (Fig. 9c), but occasionally some outline of glass shards can be observed. Sintering was followed by low temperature alteration included $SiO_2$ polymorphs (cristobalite, tridymite) and phyllosilicate mineralization reducing the permeability of the deposits (Fig. 9c, d). The remaining pores have irregular shapes and sizes (0.1–0.5 mm, Fig. 9d). The origin of the volcaniclastic material is unclear; the lower part with abundant lithics is probably connected to mass flow deposits with possible reworking. The presence of an accretionary lapilli (Fig. 8c) is an unexpected feature proving the primary pyroclastic origin (fallout component) of the upper, sintered material.

## 6. Geochemistry and mineralogy

The Lebuj lithologies have a common, high silica (74–77 wt% $SiO_2$) rhyolitic chemical composition with elevated $K_2O$ content (5 wt%, Table 2

). The rock is phenocryst poor (<5%) comprising plagioclase, sanidine, quartz with ilmenite and zircon as accessory minerals. The perlite and obsidian glass contain Fe-oxide microlites (Fig. 10a).

The micro- to crypto-crystalline groundmass with spherulites (0.2–0.5 cm, Fig. 10b) are common features of the flow and substrate rhyolites (zone $F_b$, $S_c$). Spherulites are also scattered in the sintering zone. The vapor phase crystallization and alteration included $SiO_2$ polymorphs (tridymite, cristobalite) and clay minerals attributed to the lithophysae (zone $F_b$, $S_c$) and sintered lithologies (zone $S_{cd}$). The available pore spaces were filled by cristobalite showing typical fish-scale cracking (Fig. 10c). Tridymite can be recognized in open pore spaces (Fig. 10d).

Raman mapping clearly showed mineralogical differences between the perlite, rhyolite, and the sintered lithologies (Fig. 11). The perlites were dominated by the glass (Fig. 11a, 470 $cm^{-1}$, related to the symmetric motion of bridge oxygen in Si-O-Al bonds, McMillan and Piriou, 1982). The perlite breccia matrix is colored by hematite (229, 241, 294, 405 $cm^{-1}$; Marshall et al., 2020), which also coated the onion skins of the perlitic texture (next to the breccia, see Fig. 5c). Potassium feldspar (513 $cm^{-1}$, belonging to the ring breathing mode of the $TO_4$ tetrahedron, (McKeown, 2005) was identified in the groundmass of the perlitic rhyolite (groundmass crystallization; Fig. 10b) where the contacted substrate (sintered tuff; Fig. 11b) was separated by a sharp boundary. In contrast, the quartz (463 $cm^{-1}$, belonging to the change in O-Si-O bond angle in $SiO_4$ tetrahedron; Krishnamurti, 1958) was more predominant in the sintered zone (Fig. 11b). The presence of cristobalite (228, 416

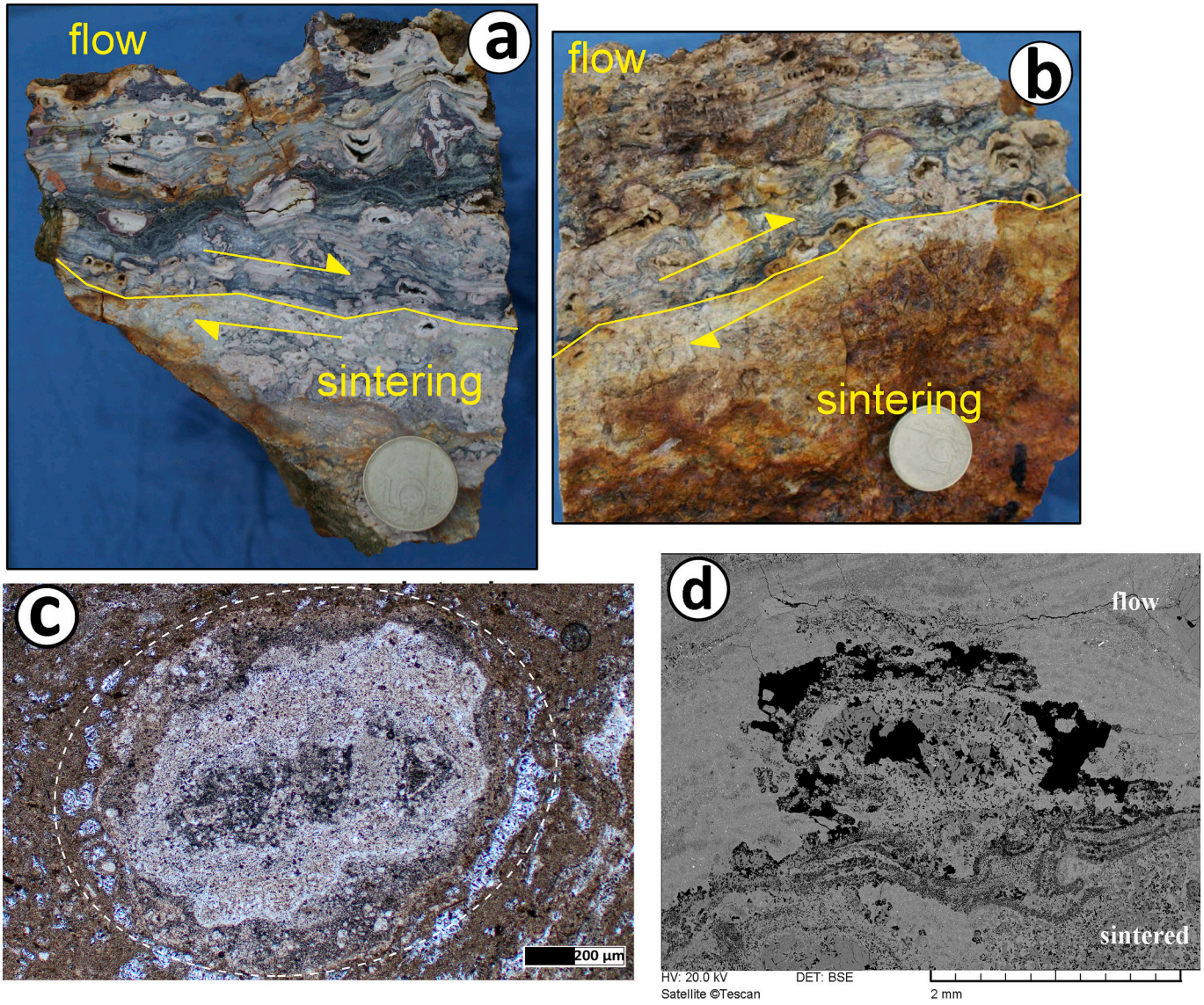


**Fig. 8.** Macro photographs, optical microscope, and BSE images of the strongly densified zone (zone $S_c$). (a-b) Lava flow ($F_b$, dark) and substrate (yellow) transition in hand specimen with well-defined texture, colour, and porosity contrast. (c) Photomicrograph in cross-polarized light (XPL) of rim-type accretionary lapilli from the sintering zone ($S_c$). (d) The BSE image of the contact plane shows grayscale contrast between the two groundmass materials: foliated flow ($F_b$, light grey) and sintered substrate ($S_c$, dark). (For interpretation of the references to colour in this figure legend, the reader is referred to the web version of this article.)

$cm^{-1}$, belonging to Si-O-Si and O-Si-O bond angle deformation modes inside the $SiO_4$ tetrahedron; Bates, 1972) and tridymite (400, 420 $cm^{-1}$, belonging to the deformational modes of Si-O-Si angle of $SiO_4$ tetrahedron; Kingma and Hemley, 1994) indicates glass devitrification and vapor phase crystallization (contact zone; Fig. 11b).

The IR absorption spectrum (Fig. 12a) indicates phyllosilicates as a glass alteration product. The smectite-rich natural clay (mixed layer kaolinite/montmorillonite or beidellite, Cuadros et al., 1994; puli.mfgi.hu) was shown to have absorption band at 3640 $cm^{-1}$ attributed to stretching vibrations of the $OH^-$ group. Another broad band at 3400 $cm^{-1}$ primarily indicates the presence of interlayered water. The amount of water in clays is related to the deformation vibrations of the H-O-H group (1660 $cm^{-1}$). These patterns are attributed to the moderately sintered pyroclast, and were also identified in samples from the contact (Fig. 12a) but absent in perlites (Fig. 12b). Other higher intensity bands between 1500 and 2000 $cm^{-1}$ can be identified as Si—O lattice vibrations of $SiO_2$ polymorphs (e.g. Biró et al., 2016) that formed during devitrification (probably cristobalite) and are also identified from Raman measurements.

### 6.1. Water content

The FTIR spectra of the glass show a large IR absorption band from 3800 to 3000 $cm^{-1}$, resulting from the fundamental O—H stretching vibrations of both molecular $H_2O$ and Si-OH and Al-OH structural groups and the overtone of H–O–H bending (Stolper, 1982; Ihinger et al., 1994). This asymmetric peak has the highest intensity for perlite (Fig. 12b) and is commonly used to determine total water concentration. The absorbance peaks at 5200 $cm^{-1}$ and 1620 $cm^{-1}$ also indicate molecular water ($H_2O_m$, H-O-H bending, Anovitz et al., 2008; Seaman et al., 2009; Renac et al., 2014, Mukasa-Tebandeke et al., 2015). The 5200 $cm^{-1}$ band intensity in the obsidian is weak and the absorbance becomes less intense (Fig. 12b). The FTIR measured glasses indicate that $H_2O_m$ is the dominant water species and the calculated water content is 0.1 and 2.2 wt% for the obsidian-perlite pair respectively. This observation is amplified further by the fact that the 4500 $cm^{-1}$ band, which is related to $OH^-$ species in glass is absent.

$H_2O$ data (Table 2) also showed the hydration effect but the range is a slightly higher (~3%) than those determined by FTIR. However, the

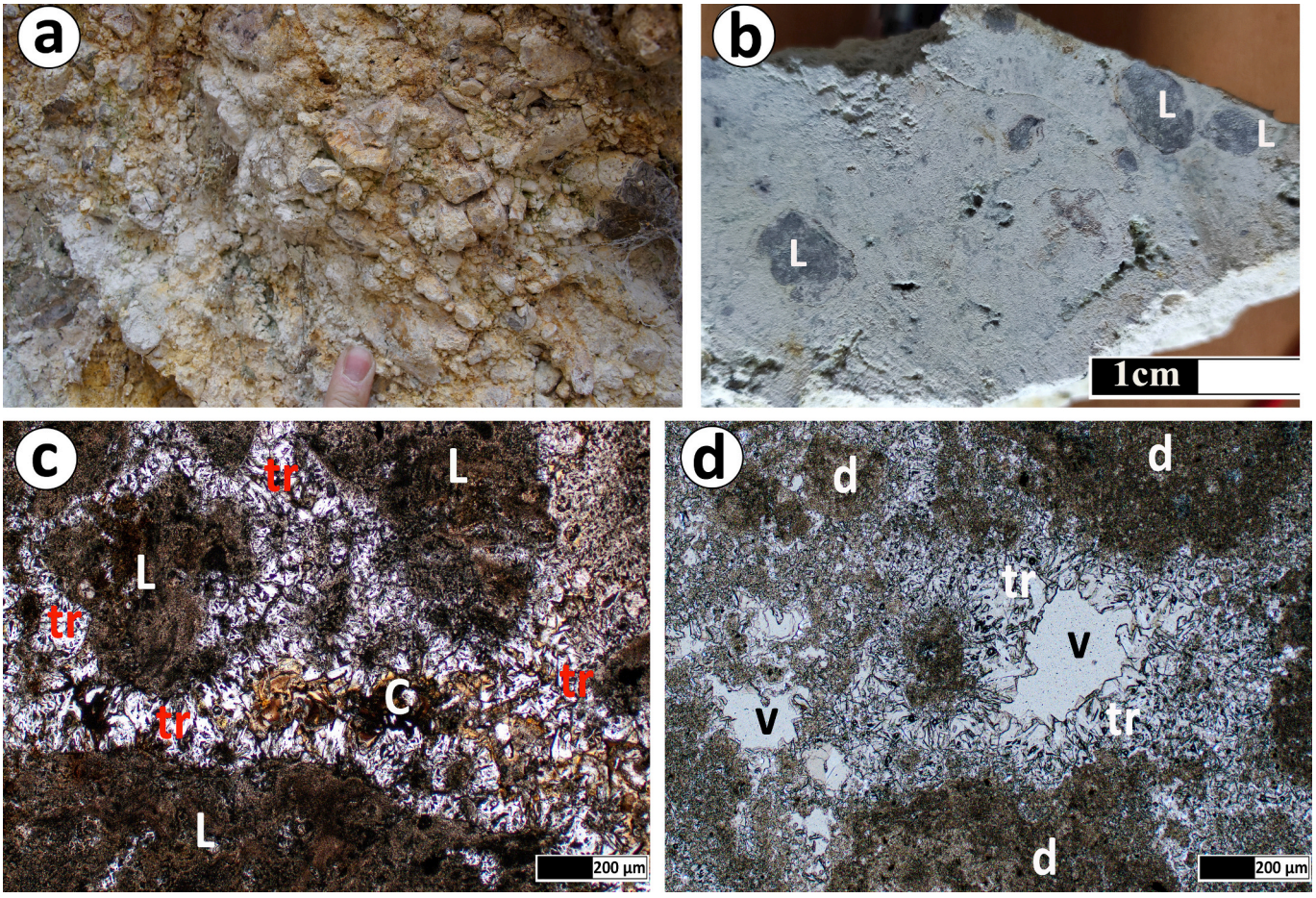


**Fig. 9.** Macro and optical microscope photographs of the moderately densified zone (zone $S_d$). (a) Yellowish-white altered clast-supported part. (b) Matrix supported texture with subangular-subrounded rhyolite lithics. (c) Photomicrograph with cross-polarized light (XPL) image of the matrix with phyllosilicate alteration (C), tridymite (tr), and rhyolite lithics (dark, L). (d) Porosity reducing tridymite partially filled the interstitial spaces (XPL) tr: tridiymite, d: devitrified crypto-crystalline domains, v: void spaces.

**Table 2**
Whole rock chemical compositions (wt%) for Lebuj and Dereszla dome samples.

| | Lebuj obsidian | Lebuj rhyolite | Lebuj perlite | Dereszla perlite |
|---|---|---|---|---|
| $SiO_2$ | 76.7 | 77.2 | 74.9 | 74.7 |
| $TiO_2$ | 0.078 | 0.081 | 0.081 | 0.074 |
| $Al_2O_3$ | 12 | 12.1 | 12 | 11.8 |
| $Fe_2O_3$ | 0.45 | 0.605 | 1.24 | 0.96 |
| FeO | 0.76 | 0.045 | 0.044 | 0.18 |
| MnO | 0.025 | 0.011 | 0.025 | 0.023 |
| CaO | 0.668 | 0.709 | 0.848 | 0.679 |
| MgO | <0.15 | <0.15 | <0.15 | <0.15 |
| $Na_2O$ | 3.19 | 3.11 | 2.79 | 2.66 |
| $K_2O$ | 5.19 | 5.34 | 4.86 | 5.26 |
| $P_2O_5$ | <0.15 | <0.15 | <0.15 | <0.15 |
| $SO_3$ | <0.15 | <0.15 | <0.15 | <0.15 |
| BaO | 0.015 | 0.019 | 0.017 | 0.006 |
| SrO | 0.002 | 0.002 | 0.002 | 0.001 |
| $H_2O^-$ | 0.05 | 0.12 | 0.13 | 0.09 |
| $H_2O^+$ | 0.56 | 0.49 | 3 | 3.48 |
| sum | 99.688 | 99.832 | 99.937 | 99.913 |

former technique analyses bulk water content where the contribution of other hydrous species (smectites, inclusions) cannot be ruled out. Therefore, the results provided by the two distinct techniques can be considered in good agreement.

## 7. Discussion

The style of silicic lava extrusion depends on several factors including viscosity, paleo-topography (pre-existing dome, crater wall), extrusion rate and defines a elongated lobes or steep-sided dome or coulee morphology (Fig. 13a; Manley, 1996; Ashwell et al., 2018; Harnett and Heap, 2021) with coherent (core) and clastic (talus) components. The relationship between high-viscosity lava and the host rocks (vent, basal shear zones) is rarely revealed in the full textural transect. In the Miocene Szerencs caldera (ca. 12 Ma), vents opened along marginal faults and formed a lava dome field (Fig. 1b,c), which is common in silicic caldera setting (e.g., Rotorua, New Zealand, Ashwell et al., 2013; Long Valley caldera, USA, Hildreth, 2004). The low water content (Fig. 12) measured on obsidian cores is evidence for a strongly degassed melt with high silica, potassium (Table 2) and low phenocryst content (<5%). The base of the Miocene Lebuj lava flow exposed a wide range of textural domains (Fig. 2, Table 1). Field observations (texture, porosity, contact features) and results of laboratory investigations are combined into a textural emplacement model (Fig. 13). The topography and the strength of substrate (e.g., crater walls, Harnett and Heap, 2021) determine the morphology and stability of lava dome growth. The key section of the Lebuj outcrop revealed a flow margin with a mixed substrate (volcaniclastics and older lava dome material) in contact (Fig. 13a). Without significant failure, the substrate was able to provide sufficient stability for the advancing flow. The dipping of flow banding is approximately parallel to the bedrock (50–70°), defining a confined flow (Fig. 13a) regime. The described textural evidences, the temperature

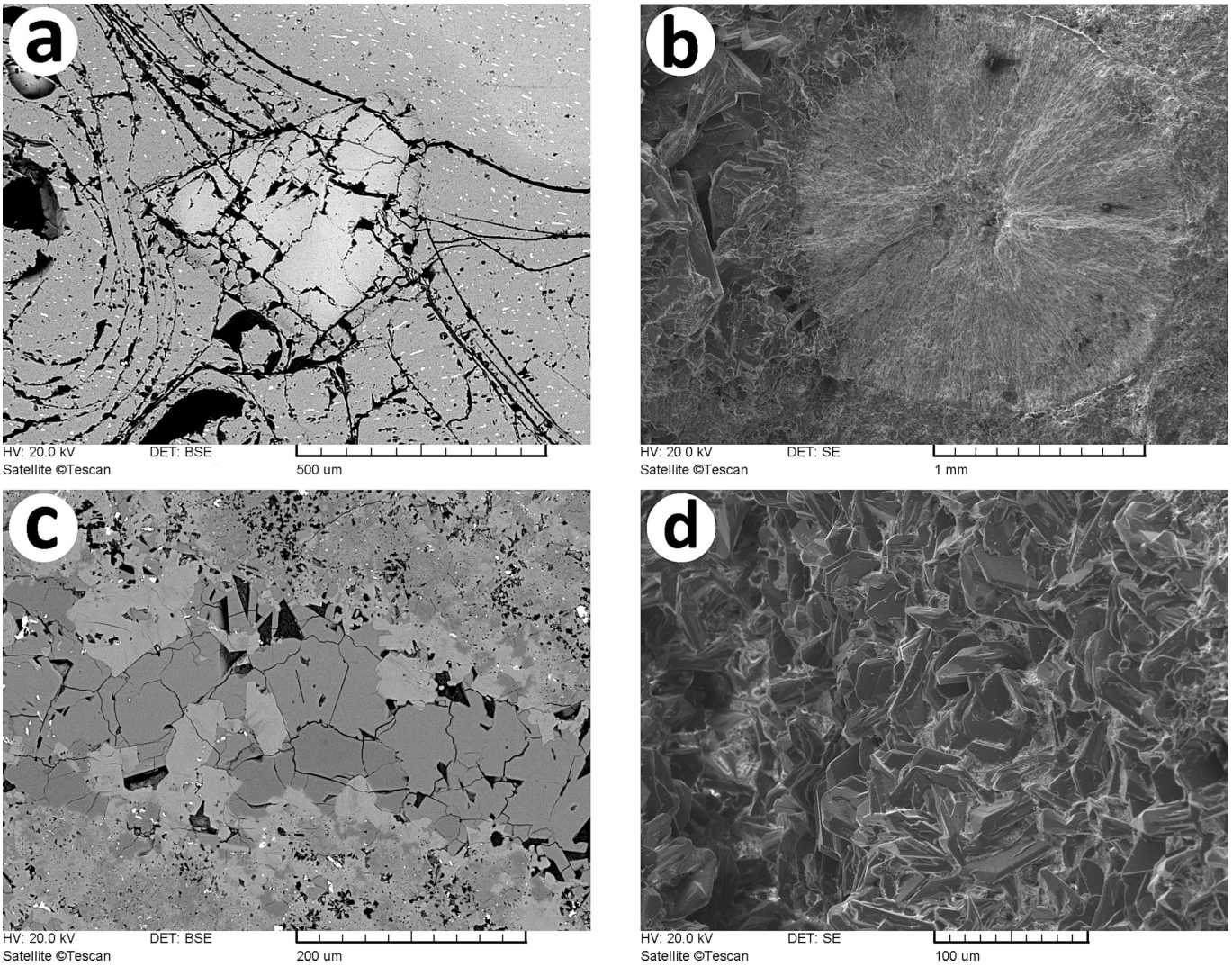


**Fig. 10.** SE and BSE images of the Lebuj mineralogy. (a) Fe oxide microlites in the glass (zone $F_a$). (b) Spherulite from the glass-microcrystalline transition (zone $F_b$). (c) Cristobalite with typical fish scale cracking (zone $S_c$). (d) Irregular intergrowth of platy silica polymorphs (crystobalite, tridymite) on lithophysae wall ($S_a$).

constraints and possible interpretation of the development processes summarized in Table 3 and Fig. 13b. The textural development of the contact zone included (1) viscous flow regime with groundmass crystallization ($F_a$) and hydration ($F_b$), (2) brittle fragmentation zone (flow: $F_c$, substrate $S_a$) (3) lithification and devitrification, substrate, $S_{c\text{-}d}$) and (4) secondary (vapor phase) mineralization processes (flow:$F_b$, substrate:$S_{a\text{-}d}$).

### 7.1. Flow emplacement and glass transition temperature

Depending on the flow/dome size and time-temperature interval above the glass transition temperature ($T_g$), a variably thickened microcrystalline core can develop in a silicic lava flow system (Fig. 13a, Manley and Fink, 1987; Stevenson et al., 1994; Furukawa et al., 2019; Szepesi, 2007). Glass transition occurs in silicate melt in a thermal interval controlled by melt chemistry (i.e., anhydrous composition, dissolved volatile content; Giordano et al., 2005) and cooling kinetics (e.g., Scarani et al., 2022). Water represents the dominant volatile species in volcanic systems and drastically reduces the glass transition temperature of the magmas. Further, during cooling, the possible increase of $H_2O$ is related to its retrograde solubility (Ryan et al., 2015), which may expand the melt window relative to the solidified glass state. This reduction in $T_g$ allows further uptake of $H_2O$ with cooling resulting in a so-called rehydration quench, which prolongs the effusion of the viscous lava body.

$T_g$ was estimated for the Lebuj flow using the chemical-based GRD model (Giordano et al., 2008; Fig. 14a) as the temperature, at which the melt viscosity corresponds to $\eta = 10^{12}$ Pa s. For our calculations, we considered the anhydrous composition of the obsidian marekanite (Table 2) as representative of primary melt, (i.e., unaffected glass phase without traces of alteration, hydration and devitrification).

The $T_g$ interval (Fig. 14a) are calculated for 0.1 and 0.2 wt% $H_2O$ content, as obtained from FTIR measurements on marekanite samples (Fig. 12) and range between 690 °C (0.2 wt% $H_2O$) and 715 °C (0.1 wt% $H_2O$). This $T_g$ range defines a lower limit for the emplacement temperatures of volcanic flows (e.g., Polo et al., 2018) and provides a thermal window (from eruptive T to $T_g$) where the pervasive groundmass and spherulite crystallization can occur. To model the timescale of viscous flow and related processes (e.g., Giordano et al., 2018; Scarani et al., 2023), a set of simulations was performed using a conductive heat transfer model (HEAT3D software; Wohletz, 1999; Wohletz et al., 1999; Di Renzo et al., 2016), also considering heat advection to the substrate during effusion and cooling. The physical, chemical and mechanical properties of the rhyolite melt and substrate (based on Romine et al., 2012) are summarized in Table 4.

In the case of Lebuj, thickened microcrystalline core has not

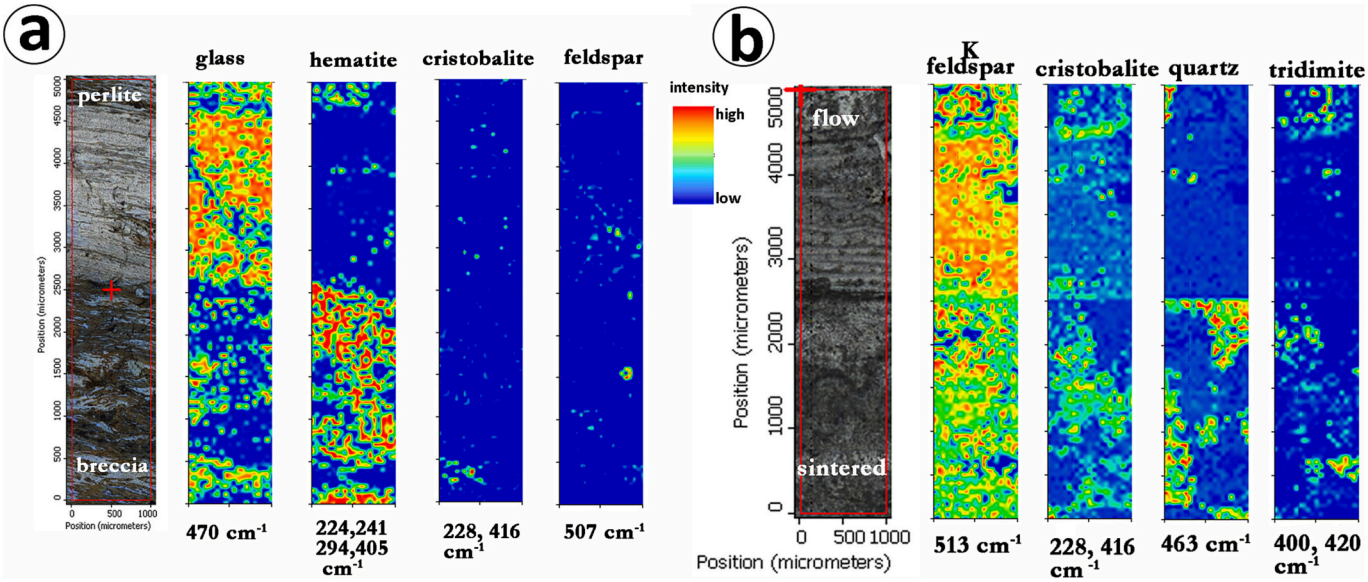


**Fig. 11.** Identified phases by Raman mapping: (a) Perlite breccia (zone $F_c$, for macro and BSE photographs, see Fig. 5). (b) Flow-sintered zone contact (zone $F_b$-$S_c$ for macro and BSE photographs, see Fig. 8).

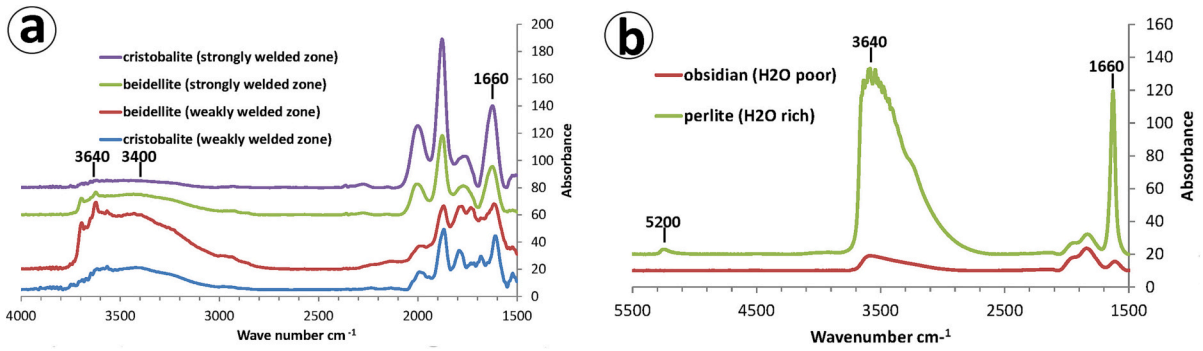


**Fig. 12.** FTIR absorption spectrum of the Lebuj lithologies. (a) flow-sintered zone contact (zone $F_b$-$S_c$, for macro and BSE photographs refer to Fig. 8). (b) perlite (zone $F_a$) with obsidian marekanite. Characteristic peaks are highlighted at 5200, 3640, 3400 and 1600 $cm^{-1}$ wavenumber positions.

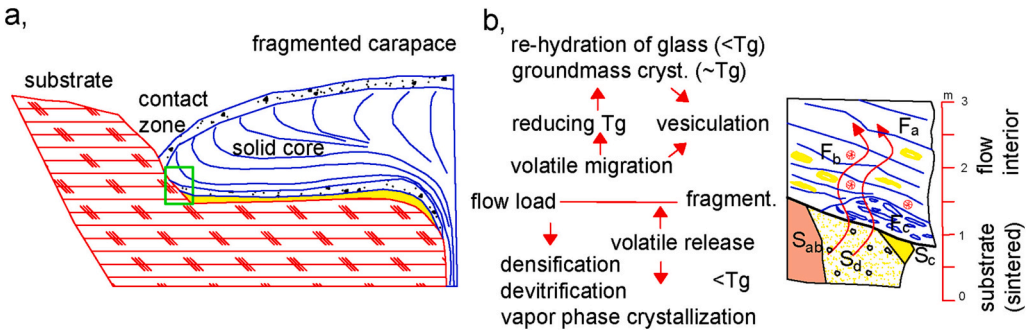


**Fig. 13.** (a) Schematic sketch of the confined flow and substrate relationship. (b) Textural evolution of the flow-substrate system including the discussed processes (Table 3).

developed (see zone $F_b$; Figs. 4, 6), the size of the microcrystalline part suggests rather a relatively small lava lobe (<100 m, Fig. 14b). Simulation results indicate that the flow interior stayed over glass transition temperature for a prolonged time (up to 10 years), which is consistent with the Banco Bonito flow simulations (< 1 °C year $^{-1}$, Kenderes et al., 2022). The substrate was also heated up to the spherulite crystallization interval (~400–500 °C; Watkins et al., 2009) as inferred from petrography (Table 1, Fig. 14c).

The lithophysae, spherulites and microcrystalline bands are textural evidence for prolonged groundmass crystallization (Manley and Fink, 1987; Breitkreuz, 2013) in the flow. The banding deformation around the microcrystalline masses and their ductile stretching, indicate that the crystallization was simultaneous with the progressive cooling of the melt above the glass transition, leading to the final relaxation of the melt (Fig. 14b). The spherulite growth is estimated to start at effective undercooling with a lower temperature limit of 400 °C (Aulock et al.,

**Table 3**
Groundmass crystallization/hydration/ /densification and low temperature mineralization textural evidences and interpretation in terms of temperature constraints and emplacement timescale.

| Process | Textural evidence | development | temperature constraints and timescale | Interpretation | References |
|---|---|---|---|---|---|
| hydration | obsidian cores in perlite | infiltration and subsequent diffusion of water deeper into the anhidrous core. | perlitized shells (~20-μm) might form in 200,000 years at 20 °C, they could form as fast as 50 years at 100 °C. | diffusion of water into glass through permeable substrate | Friedman et al., 1966 Bindeman and Lowenstern, 2016; Seligman et al., 2016, Denton et al., 2012 |
| spherulite growth | spherulite in glass (flow base and sintering zone) | the growth of spherulites requires diffusion and uptake of crystal forming components from the host rhyolite melt or glass, and rejection of non-crystal forming components from the crystallizing region. | spherulite nucleation (700–500 °C) spherulite growth: (700–500 °C) undercooling of 150 °C growth rate: 1 μm/h | diffusion controlled growth | Watkins et al., 2009, Gardner et al., 2012, Befus et al., 2015 |
| densification (sintering) | reduced porosity in the substrate | densification of the granular material and particles to coalesce, | operates where rock is held at elevated pressure and temperature (i.e., including $<T_g$) for times of hours to years. | lithification of unconsolidated volcaniclastic material | Ryan et al., 2020 |
| clay mineralization | pore filling material in the sintered substrate and lithophysae walls | glass replacement material developed by water-rock interaction | mixed clay structure indicates medium to low alteration degree estimated temperature between 50 and 100 °C | weak acidic alteration material reducing permeability | Cuadros et al., 1994, Ball et al., 2015 |
| tridymite/ cristobalite/ mineralization | | silica polymorphs are growing into open pore spaces and fractures as vapor phase fluids passing through the permeable lithologies | 'fish scale' cracking (Fig. 10c) that is attributed to a volume reduction experienced during the ~240 °C displacive β (cubic) → α (tetragonal) transition | silica maybe transported into dome from outside sources e.g. incorporated meteoric waters | Horwell et al., 2013, Schipper et al., 2020 |

2013; Watkins et al., 2009), which may take a prolonged interval (up to years) under moderate heat loss conditions.

The lithophysae structures (Fig. 4) revealed a complex crystallization history. Their growth also distorts the banding with semicircular, upward bulging cavities (Fig. 4c). The larger (up to dm) structures have concentric edges reflecting crystallization pulses with a moving volatile saturation front (Breitkreuz, 2013). Their minerals are the same as in the sintering zone (tridymite, cristobalite) connected to silica redistribution in the cooling lava dome.

### 7.2. Hydration

The obsidian marekanite in the perlite was already identified by early neptunist-plutonist workers (Townson, 1797; Esmark, 1798; Szabó, 1867) recording an incomplete hydration process (Fig. 3d). The presence of marekanite is an important feature since in the TSM as many perlite deposits are fully hydrated and lack relict obsidian (Szepesi et al., 2018, 2019). The obsidian cores and surrounding perlite have an oriented, banded texture (Fig. 3), indicating ductile stretching of the glass under basal shear conditions. The onion-like perlitic fracturing intersect the banding planes, indicating that the hydration postdates the fluidal stretching and developed after movement has ceased. At ambient conditions the diffusion is slow ($5 \times 10^{-5}$ cm$^2$/million years, Friedman et al., 1966), so the obsidians grains can be preserved in younger (e.g., Pleistocene Yellowstone, USA, Bindeman and Lowenstern, 2016; El Viejo, Argentina, Bustos et al., 2020) and Miocene geological settings (e.g., NW Mexico: Vidal-Solano et al., 2008, other Carpathian glasses, Kohút et al., 2021).

The FTIR and BSE investigations demonstrate that there are sharp transitions from the hydrated ~3 wt% perlitic rims to non-hydrated obsidian cores (Fig. 3d). Bindeman and Lowenstern (2016) interpreted this pattern as a quenched "hydration front", where the diffusion coefficients are strongly dependent on water concentrations. The load of a lava flow of 100 m thickness would produce a stress of ~2.5 MPa (Fig. 14a). The high water content in perlites would be in equilibrium at $T_g$ at ~20 MPa (i.e. ~1000 m lava thickness). These unrealistic values may suggest that hydration occur below $T_g$. The hematite coating in the perlite skins (zone $F_c$; Fig. 5c) indicates that the textural water diffusion occurred before the last oxidation event. An $H_2O$ diffusional closure of 60–100 °C was estimated for perlites from the Yellowstone caldera (Bindeman and Lowenstern, 2016) which contained 2–3 wt% water content. In the $Fe_2O_3$ -$H_2O$ system, hematite stability temperatures can drop near 100 °C (Tareen and Krishnamurthy, 1981), consistent with this low-temperature hydration interval (Anovitz et al., 2008; Bindeman and Lowenstern, 2016).

The origin of the water in the hydration process is essentially meteoric but the direction of the fluid flux can be supplied through the dome (downward) or upwelling from substrate (bottom up). The Table 5 summarizes Pleistocene and Miocene perlite deposits (references therein) containing obsidians nodules with referring to the $H_2O$ content and hydrational environment. The origin of the water was synglacial in the recent (Yellowstone, Iceland) or surface meteoric in the case of the older glasses (Carpathians). The Lebuj perlites contains lower $H_2O$ (<3%, Table 2) than Pleistocene perlites and other Carpathian localities (3–5%; Szepesi et al., 2015; Lexa et al., 2021). This is consistent with the size of volcanic body and basal position inside the flow. The downward fluid flux through the solid core (over 50 m) does not provide sufficient infiltration of water for hydration and alteration processes (Ball et al., 2015) so this must have been related to the substrate (Fig. 13b). A humid climate characterized the Miocene environment of the Szerencs caldera. The volcaniclastic deposits hosted significant aquifers with surface runoff, lakes and related hydrothermal circulation (Pécskay and Molnár, 2002). According to this, the mixed substrate was permeable at time of the effusion but the amount of available water did not reach the minimum required for fluidization and soft sediment deformation (e.g., McLean et al., 2016). According to the fluid exchange model beneath silicic lava domes (Ball et al., 2015), the water – rock interaction resulted in weak hydrothermal alteration of the substrate and water flux to the quenched glass. As an interaction of the two processes the increased sintering and mineralization reduced the porosity of the substrate forming an impermeable barrier (Riehle et al., 2010), which reduced further water uptake for hydration. Thus, the marekanite is probably the result of a "quenched" hydration front (Bindeman and Lowenstern, 2016). The $H_2O$ diffusion after the formation of the sintering zone and hydration front clearly cannot be excluded, but the diffusion rate must be slowed down.

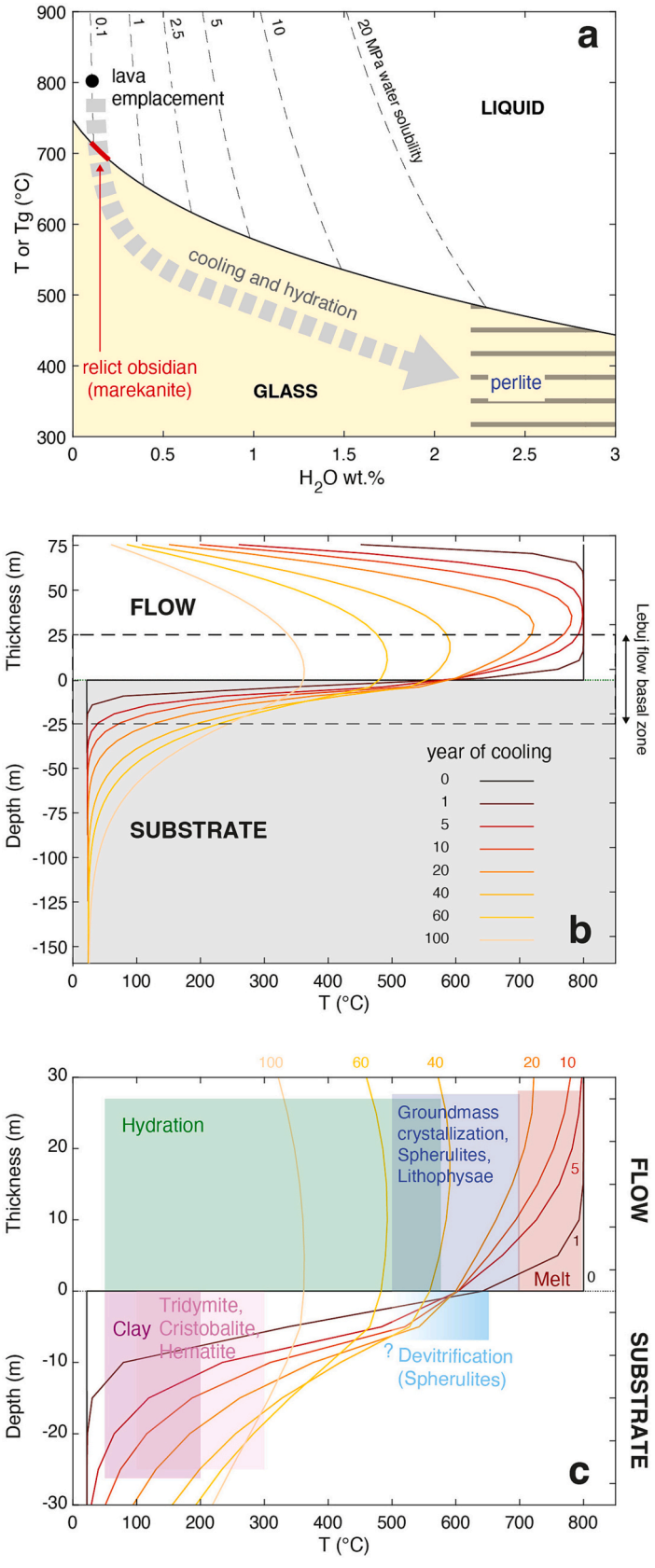


**Fig. 14.** Model isobaric (0.1–20 MPa) hydration-cooling paths in volcanic systems and corresponding glass transition temperatures ($T_g$; Based on Ryan et al., 2015). The solubility curves (dashed lines) predicted by Liu et al. (2005) model and plotted as T (°C) vs. $H_2O$ content (wt%) for a range of P (numbers on lines, in MPa). Glass transition temperature ($T_g$, red line) of the relict obsidian (0.1 wt% $H_2O$) are calculated using the GRD model. The schematic grey arrow indicated cooling and hydration path below $T_g$. (b) 2D conductive/convective numerical modeling results for a smaller lava lobe with a thickness of < 100 m by HEAT3D code (Wohletz, 1999; Wohletz et al., 1999; Di Renzo et al., 2016) showing sequential temperature curves of cooling. Rhyolite and bedrock properties used in the calculation are listed in Table 4 (based on Romine et al., 2012). Lines indicate the elapsed cooling time. (c) Estimated timescale and temperature windows for the hydration and mineralization processes during the cooling to ambient temperature. Enlargement of the HEAT3D modeling results (Fig. 14b). (For interpretation of the references to colour in this figure legend, the reader is referred to the web version of this article.)

**Table 4**
Starting parameters of the rhyolitic glass (flow) and substrate from Romine et al. (2012) and used for the HEAT 3D thermal modeling.

| | K (W/m K) | Cp (J/kg K) | Density | Porosity | $T_0$ °C |
|---|---|---|---|---|---|
| rhyolitic glass | 1.5 | 1375 | 2350 | – | 800 |
| substrate | 1.2 | 1000 | 1500 | 50% | – |

### 7.3. Flow-substrate interaction 1: fragmentation

Lava substrate interactions are rarely observed in nature and the thermo-mechanical contact reported mainly from basaltic lava flows (Fagents and Greeley, 2001; Williams et al., 2004; Gallant et al., 2020). A basal shear zone is common in effusive silicic volcanism (Manley and Fink, 1987; Guimarães et al., 2018; Smith, 1996; Szepesi et al., 2019). The isolated breccia lenses of the upper lava flow at the contact imply that fragmentation occurred mainly due to the local mechanical stress rather than thermal influence (Smith, 1996). The shearing supported the fragmentation, which decreased in intensity upwards into intact lava. This brittle-ductile transition was coupled with minor vesiculation (Fig. 5d), increasing porosity.

The subordinate clastic components (zone $F_c$ and $S_b$, Figs. 2, 5, 7) are important features of the Lebuj succession. Heap and Violay (2021) summarized the mechanical behavior and failure modes of the volcanic rocks. The brittle behavior is typically characterized by shear fracture formation and increased porosity, as opposed to ductile deformation style. These processes are observable 'in situ' in the perlite breccia, where the texture is fractured along microcracks (Fig. 5c) and elevated porosity developed by fragmentation and vesiculation (Fig. 5d). The perlite breccia was probably a basal autobreccia (Fig. 13 a, b). The shear induced deformation (Fig. 5a, b) distorted the black glass into flame-like lenticular lenses. This textural fabric is common in the basal shear zone of effusive silicic volcanism (Smith, 1996; Bull and McPhie, 2007).

The other fragmented lithofacies was the hard substrate rhyolite ($S_b$, Figs. 6a, 7). This occasional contact was also caused by brittle fragmentation at the substrate/flow interface, and the breccia is oriented parallel to the extrusion direction. Besides the minor clast rotation and alignment, clast flattening did not really occur (Fig. 7b). The lithics also incorporated to perlite breccia (Fig. 5b). This setting probably connected to mechanical erosion of steep channel wall (Fig. 6a) as reported from basalt – dacite interaction from Mount St. Helens (Williams et al., 2004). The higher porosity of the breccia is caused by moderate densification of the solid microcrystalline material under the pressing and heating of overlying flow.

### 7.4. Flow-substrate interaction 2: lithification and sintering

The Lebuj flow lava was also in contact with the volcaniclastic substrate (Figs. 6,8,9,13) and this material behaved differently from the rigid rhyolite. If a fragmental volcaniclastic deposits may hot enough can relax viscously (above $T_g$, Wadsworth et al., 2016) as have been described mainly from block and ash flow deposits (Alarcón et al., 2020), ignimbrites (Streck and Grunder, 1995; Ellis et al., 2015) and shallow conduits (Vasseur et al., 2013). But densification and mineralization processes can also take place at lower temperatures and the granular beds accompanies transition to an impermeable densified state (Wadsworth et al., 2016).

The microstructural evidences proved that and the lithification of glass resulted in development of a density profile with high ($S_c$, Fig. 8) to moderate ($S_d$, Fig. 9) rank of compaction. The heat flux, movement and pressing of the rhyolite flow including pervasive devitrification destroyed the former, probably glassy texture (e.g. Fig. 8) causing permeability loss in the neighboring 50 cm zone ($S_c$, high densification rank, Figs. 2, 6b, d, 8). Further away from the contact zone, the rate of lithification decreases (moderate to high densification rank), and porosity-reducing secondary mineralization can be identified (Figs. 9c, d;10c, d). Water from the substrate as dominant volatile species can also affect the temperature limit of the devitrfication and spherulite crystallization processes. General calculation of the flow emplacement conditions (Heat 3D model, Fig. 14b, c) indicated elevated temperature estimates of the substrate. Ryan et al. (2020) discussed three different ways for granular material densification: a, viscous sintering (above $T_g$), solid state sintering (below $T_g$) and fluid accelerated densification. Our case can be explained by the latter. The combined heat and hot pressing (Ryan et al., 2018) at the flow base combining with precipitation of mineral phases were enough for the lithification of the unconsolidated volcaniclastic material. Based on the devitrification textures, the upper temperature limit of the sintering timescale is already in the range of spherulite crystallization (Fig. 14c). The substrate reheating and cooling estimates are also similar to spherulite-based cooling rate calculations (month-year, Watkins et al., 2009). Similar crystallization pattern described from Rattlesnake Tuff (Oregon, USA, Streck and Grunder, 1995), where the crystallization facies includes vapor phase, pervasively devitrified, spherulite and lithophysae zone.

On a wider scale, a special growth pattern and core/substrate interface of natural domes are described here. The lithification of volcaniclastic rocks during flow emplacement is an important process to be fully understood. The sintered material can be used to infer slow extrusion rate, which affects the texture, promoting fluid-rock interaction. The reduction of substrate permeability, act as impermeable barrier has been invoked as a factor that modulates flow emplacement or magma outgassing during conduit ascent (e.g., Kennedy et al., 2010)

### 7.5. Mineralization

The vapor phase crystallization caused mineral precipitation in the dome rock and the sintering zone. The BSE imaging, the Raman mapping, and the FTIR spot measurement revealed the complex syn and post-emplacement mineralogy of the deposits. The crystalline silica polymorphs of cristobalite, quartz, and tridymite are frequent components of lava domes (Horwell et al., 2010, 2013). K-feldspar is also common in the felsitic groundmass and the spherulites (Rowe et al.,

**Table 5**
Interpretation and origin of water in the hydration process from Pleistocene and Miocene localities; O:obsidian, P: perlite.

| Occurence | | Age | Lithofacies | $H_2O$ content | Origin of water | References |
|---|---|---|---|---|---|---|
| Yellowstone | | Pleistocene | obsidian cores, perlite, microcrystalline and altered lavas | O:0.1–0,0.3% P:1–3% | secondary hydration by synglacial meltwater | Bindeman and Lowenstern, 2016 |
| Iceland (Krafla, Torfajökull) | | Pleistocene | obsidian, perlitic spherulitic, pumiceous obsidian, breccia, | O:0.44–2.05% P:2.15–8.15% | subglacial hydration | Denton et al., 2009, 2012 |
| Slovakia | Jastraba, Lehotka p. Brehmi | Miocene | no obsidian cores, dense and pumiceous perlite 3,7-5,1% | P: 3.5–5.1% | hydration by meteoric water | Varga et al., 2019, Lexa et al., 2021, Bačo et al., 2018 |
| | Vinicky | | obsidian cores, dense and brecciated perlite | O: 0.1% P: 3% | | |
| Tokaj Mts | Telkibánya-Pálháza | Miocene | no obsidian, pumiceous, brecciated, dense and spherulitic perlite | P:2.78–4.25% | hydration by meteoric water | Rózsa et al., 2006, Szepesi et al., 2015 |
| | Erdőbénye, Olaszliszka | | obsidian cores up to dm size, dense perlite | O:0.22–0.57% P:3.0–3.17% | | |

2012, Aulock et al. 2013, Watkins et al., 2009). The phyllosilicates are connected only to the sintered (Figs. 8c, 12a) sections. This mineralization pattern is common in lava domes and is formed by vapor transport/deposition and devitrification (Ball et al., 2015). Silica polymorphs are observed growing into open pore spaces and fractures (Figs. 9 cd,10 cd) and are interpreted as vapor phase fluids passing through the permeable lithologies (Ball et al., 2013; Horwell et al., 2013). Cristobalite crystals usually have the characteristic"fish scale" cracking (Fig. 10c) that is attributed to a volume reduction experienced during the ~240 °C displacive β (cubic) → α (tetragonal) transition (Horwell et al., 2013; Schipper et al., 2020).

Phyllosilicates are also useful mineral assemblages for predicting alteration conditions. The smectite group minerals typically record acidic type alteration, where the water-rock interaction commonly produces glass replacement minerals (Caballero et al., 2005). The FTIR-identified mixed clays indicate low- to-medium alteration degree (estimated temperature between 50 and 100 °C) parallel with the low-temperature hydration window of perlite (Anovitz et al., 2008; Bindeman and Lowenstern, 2016). This secondary mineralization also plays a fundamental role in decreasing the porosity and increasing the rock strength forming a strongly cohesive substrate. At the edifice scale, the mechanical behavior and failure modes of volcanic rock is not yet well understood. The fragmentation and volatile exsolution events can cause volcano instability, while progressive vapor phase mineralization would tend to increase rock strength (Heap and Violay, 2021). The volcanic flank/dome strength profiles need field-based information but the basal shear zones cannot be studied directly under an active flow/-dome complex.

## 8. Conclusions

Textural evidences suggest that the following series of events occurred at the Lebuj flow base: *a,* a viscous rhyolite flow advanced on an irregular topography, *b,* shear concentrated along the side of the paleo-valley, *c,* brittle fracturing occurred at the contact (both in the lava and hard substrate), *d,* groundmass crystallization and hydration acted parallel to the melt glass transition boundary layer (690–710 °C, Fig. 14b) in the ductile flow, *e,* variable scale densification occurred in the substrate (below $T_g$) followed by low temperature mineralization.

The substrate breccia and its incorporated lithics show evidence of mechanical contact along the steep channel wall. Although the flow remains above the glass transition temperature, there is no evidence that this would be sufficient to cause typical welding by viscous sintering in the volcaniclastic material. The development of the described substrate compaction profile preceded the flow driven low temperature mineralization processes. The precipitation of $SiO_2$ polymorphs and phyllosilicate minerals was consistent with the flow hydration window model (Bindeman and Lowenstern, 2016100–250 °C, Fig. 14b) The meteoric water was derived from pyroclastic dominated caldera succession and migrated upward. This bottom up model has also been described for ignimbrites (Self et al., 2022), where similar hydrothermal alteration documented. Using the time-temperature-porosity information given by this reconstruction, we suggest special densification and lithification of the volcaniclastic material under a cooling lava flow. This relative timescale for textural development provided by reconstruction of lava flow and substrate interaction.

## Funding

This research has been funded by the Hungarian–Italian MTA-CNR bilateral research project 2019–2022 (led by S. Harangi and G. Groppelli). The research was also supported by the European Union and the State of Hungary, financed by the European Regional and Development Fund in the project of GINOP-2.3.2-15-2016-00009 'ICER' project, and co-financed by the National Research, Development and Innovation Office–NKFIH No. 131869 OTKA project. We also acknowledge the financial support of the Water in the fire K128122 NKFIH grant, and the infrared laboratory of the Forensic Institute for Physics and Chemistry. RL was supported by the Bolyai János Research Fellowship.

## CRediT authorship contribution statement

**János Szepesi:** Conceptualization, Methodology, Investigation, Writing – original draft, Writing – review & editing. **Alessandro Vona:** Conceptualization, Methodology, Investigation, Writing – original draft, Writing – review & editing. **István János Kovács:** Methodology, Investigation. **Krisztián Fintor:** Methodology, Investigation. **Kata Molnár:** Methodology, Investigation. **Alex Scarani:** Methodology, Investigation, Writing – review & editing. **Guido Giordano:** Conceptualization. **Réka Lukács:** Conceptualization, Writing – original draft.

## Declaration of Competing Interest

The authors declare no competing interests.

## Data availability

No data was used for the research described in the article.

## Acknowledgement

The authors would like to thank Timothy Jull for constructive criticism of the manuscript. The first author would like to thank Miklós Kozák for his long professional collaboration and assistance with fieldwork and sample processing. We would like to thank Amy Ryan and an anonymous reviewer for their useful comments and suggestions, which helped us to make improvements to the manuscript.

## References

Alarcón, E., Murcia, H., Borrero, C., et al., 2020. Evidence for welding of a block and ash pyroclastic flow deposit: the case of Cerro Bravo Volcano, Colombia. Bull. Volcanol. 82, 3. https://doi.org/10.1007/s00445-019-1334-5.

Anovitz, L.M., Cole, D.R., Fayek, M., 2008. Mechanisms of rhyolitic glass hydration below the glass transition. Am. Mineral. 93, 1166–1178. https://doi.org/10.2138/am.2008.2516.

Ashwell, P., Kennedy, B.M., Gravley, D.M., von Aulock, F.W., Cole, J.W., 2013. Insights into caldera and regional structures and magma body distribution from lava domes at Rotorua Caldera, New Zealand. J. Volcanol. Geotherm. Res. 258, 187–202. https://doi.org/10.1016/j.jvolgeores.2013.04.014.

Ashwell, P.A., Kennedy, B.M., Edwards, M., et al., 2018. Characteristics and consequences of lava dome collapse at Ruawahia, Taupo Volcanic Zone, New Zealand. Bull. Volcanol. 80, 43. https://doi.org/10.1007/s00445-018-1217-1.

Aulock, F.W., Nichols, A.R.L., Kennedy, B.M., Oze, C., 2013. Timescales of texture development in a cooling lava dome. Geochim. Cosmochim. Ac. 114, 72–80. https://doi.org/10.1016/j.gca.2013.03.012.

Bačo, P., Lexa, J., Bačová, Z., Konečný, P., Pécskay, Z., 2018. Geological background of the occurrences of Carpathian volcanic glass, mainly obsidians. In: Eastern Slovakia Archeometriai Műhely, XV(3), pp. 157–166.

Ball, J.L., Calder, E.S., Hubbard, B.E., Bernstein, M.L., 2013. An assessment of hydrothermal alteration in the Santiaguito lava dome complex, Guatemala: Implications for dome collapse hazards. Bull. Volcanol. 75, 1–18. https://doi.org/10.1007/s00445-012-0676-z.

Ball, J.L., Stauffer, P.H., Calder, E.S., Valentine, G.A., 2015. The hydrothermal alteration of coolinglava domes. Bull. Volcanol. 77, 1–16. https://doi.org/10.1007/s00445-015-0986-z.

Bates, J.B., 1972. Raman spectra of α and β Cristobalite. J. Chem. Phys. 57 (9), 4042–4047.

Befus, K.S., Watkins, J., Gardner, J.E., et al., 2015. Spherulites as in-situ recorders of thermal history in lava flows. Geology 43, 647–650. https://doi.org/10.1130/G36639.1.

Bindeman, I.N., Lowenstern, J.B., 2016. Low-δD hydration rinds in Yellowstone perlites record rapid syneruptive hydration during glacial and interglacial conditions. Contrib. Mineral. Petrol. 171, 89. https://doi.org/10.1007/s00410-016-1293-1.

Biró, T., Kovács, I.J., Király, E., Falus, G., et al., 2016. Concentration of hydroxyl defects in quartz from various rhyolitic ignimbrite horizons: results from unpolarized micro-FTIR analyses on unoriented phenocryst fragments. Eur. J. Mineral. 28, 313–327. https://doi.org/10.1127/ejm/2016/0028-2515.

Breitkreuz, C., 2013. Spherulites and lithophysae-200 years of investigation on high-temperature crystallization domains in silica-rich volcanic rocks. Bull. Volcanol. 75, 1–16. https://doi.org/10.1007/s00445-013-0705-6.

Bull, K.F., McPhie, J., 2007. Fiamme textures in volcanic successions: Flaming issues of definition and interpretation. J. Volcanol. Geotherm. Res. 164, 205–216. https://doi.org/10.1016/j.jvolgeores.2007.05.005.

Bustos, E., Báez, W.A., Bardelli, L., et al., 2020. Genesis of megaspherulites in El Viejo Rhyolitic Coulee (Pleistocene), Southern Puna, Argentina. Bull. Volcanol. 82, 43. https://doi.org/10.1007/s00445-020-01382-8.

Caballero, E., Jiménez De Cisneros, C., Huertas, F.J., Huertas, F., Pozzuoli, A., Linares, J., 2005. Bentonites from Cabo de Gata, Almería, Spain: a mineralogical and geochemical overview. Clay Minerals 40, 463–480. https://doi.org/10.1180/0009855054040184.

Castro, J., Cashman, K., Joslin, N., Olmsted, B., 2002. Structural origin of large gas cavities in the big Obsidian Flow, Newberry Volcano. J. Volcanol. Geotherm. Res. 114, 313–330. https://doi.org/10.1016/S0377-0273(01)00296-7.

Cuadros, J., Delgado, A., Cardenete, A., Reyes, E., Linares, J., 1994. Kaolinite / montmorillonite resembles beidellite. Clay Clay Miner. 42 (5), 643–651. https://doi.org/10.1346/CCMN.1994.0420517.

Denton, J.S., Tuffen, H., Gilbert, J.S., Odling, N., 2009. The hydration and alteration of perlite and rhyolite. J. Geol. Soc. Lond. 166, 895–904. https://doi.org/10.1144/0016-76492008-007.

Denton, J.S., Tuffen, H., Gilbert, J.S., 2012. Variations in hydration within perlitised rhyolitic lavas-evidence from Torfajökull, Iceland. J. Volcanol. Geotherm. Res. 223–224, 64–73. https://doi.org/10.1016/j.jvolgeores.2012.02.005.

Di Renzo, V., Wohletz, K., Civetta, L., Moretti, R., Orsi, G., Gasparini, P., 2016. The thermal regime of the Campi Flegrei magmatic system reconstructed through 3D numerical simulations. J. Volcanol. Geotherm. Res. 328, 210–221. https://doi.org/10.1016/j.jvolgeores.2016.11.004.

Ellis, B.S., Cordonnier, B., Rowe, M.C., et al., 2015. Groundmass crystallisation and cooling rates of lava-like ignimbrites: the Grey's Landing ignimbrite, southern Idaho, USA. Bull. Volcanol. 77, 87. https://doi.org/10.1007/s00445-015-0972-5.

Esmark, I., 1798. Kurze Beschreibungen einer mineralogische Reise durch Ungarn, Siebenbürgen und das Bahnat. Freiberg.

Fagents, S.A., Greeley, R., 2001. Factors influencing lava-substrate heat transfer and implications for thermomechanical erosion. Bull. Volcanol. 62, 519–532. https://doi.org/10.1007/s004450000113.

Friedman, I., Smith, R.L., 1958. The deuterium content of water in some volcanic glasses. Geochim. Cosmochim. Acta 15. https://doi.org/10.1016/0016-7037(58)90059-0.

Friedman, I., Smith, R.L., Long, W.D., 1966. Hydration of natural glass and formation of perlite. GSA Bull. 77 (3), 323–328.

Furukawa, K., Uno, K., Kanamaru, T., Nakai, K., 2019. Structural variation and the development of thick rhyolite lava: A case study of the Sanukayama rhyolite lava on Kozushima Island, Japan. J. Volcanol. Geotherm. Res. 369, 1–20. https://doi.org/10.1016/j.jvolgeores.2018.11.001.

Gallant, E., Deng, F., Connor, C.B., et al., 2020. Deep and rapid thermo-mechanical erosion by a small-volume lava flow. Earth Planet. Sci. Lett. 537, 116163 https://doi.org/10.1016/j.epsl.2020.116163.

Gardner, J.E., Befus, K.S., Watkins, J., et al., 2012. Compositional gradients surrounding spherulites in obsidian and their relationship to spherulite growth and lava cooling, 74, pp. 1865–1879. https://doi.org/10.1007/s00445-012-0642-9.

Giordano, D., Nichols, A.R.L., Dingwell, D.B., 2005. Glass transition temperatures of natural hydrous melts: a relationship with shear viscosity and implications for the welding process. J. Volcanol. Geotherm. Res. 142, 105–118. https://doi.org/10.1016/j.jvolgeores.2004.10.015.

Giordano, D., Russell, J.K., Dingwell, D.B., 2008. Viscosity of magmatic liquids: A model. Earth Planet. Sci. Lett. 271, 123–134. https://doi.org/10.1016/j.epsl.2008.03.038.

Giordano, G., Zanella, E., Trolese, M., Baffioni, C., Vona, A., Caricchi, C., De Benedetti, A. A., Corrado, S., Romano, C., Sulpizio, R., Geshi, N., 2018. Thermal interactions of the AD79 Vesuvius pyroclastic density currents and their deposits at Villa Dei Papiri (Herculaneum archaeological site, Italy). Earth Planet. Sci. Lett. 490, 180–192. https://doi.org/10.1016/j.epsl.2018.03.023.

Guimarães, L.F., De Campos, C.P., Janasi, V.A., et al., 2018. Flow and fragmentation patterns in the silicic feeder system and related deposits in the Paraná-Etendeka Magmatic Province, São Marcos, South Brazil. J. Volcanol. Geotherm. Res. 358, 149–164. https://doi.org/10.1016/j.jvolgeores.2018.03.021.

Gyarmati, P., 1977. A Tokaji-hegység intermedier vulkanizmusa. Ann. Hung. Geol. Inst. 55, 1–195 (in Hungarian).

Harnett, C.E., Heap, M.J., 2021. Mechanical and topographic factors influencing lava dome growth and collapse. J. Volcanol. Geotherm. Res. 420, 107398 https://doi.org/10.1016/j.jvolgeores.2021.107398.

Heap, M.J., Violay, M.E.S., 2021. The mechanical behaviour and failure modes of volcanic rocks: a review. Bull. Volcanol. 83, 33. https://doi.org/10.1007/s00445-021-01447-2.

Hegedűs, E., Posgay, K., Bodoky, T., Fancsik, T., Kovács, A.C., Csabafi, R., Celebration Working Group, 2002. 3D refraction tomographic images from the Mátra–Zemplén region. – Geologica Carpathica 53 Special CD Issue. In: Proceedings of XVII. Congress of Carpathian–Balkan Geological Association Bratislava, September 1st – 4th 2002.

Hildreth, W., 2004. Volcanological perspectives on Long Valley, Mammoth Mountain, and Mono Craters: several contiguous but discrete systems. J. Volcanol. Geotherm. Res. 136, 169–198. https://doi.org/10.1016/j.jvolgeores.2004.05.019.

Horwell, C.J., Le Blond, J.S., Michnowicz, S.A.K., Cressey, G., 2010. Cristobalite in a rhyolitic lava dome: Evolution of ash hazard. Bull. Volcanol. 72, 249–253. https://doi.org/10.1007/s00445-009-0327-1.

Horwell, C.J., Williamson, B.J., Llewellin, E.W., et al., 2013. The nature and formation of cristobalite at the Soufrière Hills volcano, Montserrat: implications for the petrology and stability of silicic lava domes. Bull Volcanol 75, 696. https://doi.org/10.1007/s00445-013-0696-3.

Ihinger, P.D., Hervig, R.L., McMillan, P.F., 1994. Analytical methods for volatiles in glasses. In: Carroll, M.R., Holloway, J.R. (Eds.), Volatiles in Magmas. Reviews in Mineralogy, vol. 30. Mineralogical Society of America, Washington, D.C, pp. 67–121.

Karátson, D., Timár, G., 2005. Comparative volumetric calculations of two segments of the Carpathian Neogene/Quaternary volcanic chain using SRTM elevation data: implications to erosion and magma output rates. Zeitschrift für Geomorphologie, Suppl.-Bd. 140, 19–35.

Kenderes, S.M., Befus, K.S., Bryson, A.N., Whittington, A.G., 2022. Thermal histories and emplacement dynamics of rhyolitic obsidian lavas at Valles caldera, New Mexico. Bull. Volcanol. 1–18 (84), 98. https://doi.org/10.1007/s00445-022-01606-z.

Kennedy, B.M., Jellinek, A.M., Russell, J.K., Nichols, A.R.L., Vigouroux, N., 2010. Time- and temperature-dependent conduit wall porosity: a key control on degassing and explosivity at Tarawera volcano, New Zealand. Earth Planet. Sci. 299 (1–2), 126–137. https://doi.org/10.1016/j.epsl.2010.08.028.

Kingma, K.J., Hemley, R.J., 1994. Raman spectroscopic study of microcrystalline silica. Am. Mineral. 79, 269–273.

Kiss, P., Gméling, K., Molnár, F., Pécskay, Z., 2010. Geochemistry of Sarmatian volcanic rocks in the Tokaj Mts (NE Hungary) and their relationship to hydrothermal mineralization. Cent. Eur. Geol. 53, 377–403. https://doi.org/10.1556/ceugeol.53.2010.4.3.

Kohút, M.C., Sherlock, S.M., Halton, A., 2021. The 40Ar–39Ar dating and geochemistry of the Carpathian C1 obsidians (Zemplín, Slovakia). Geol. Carpath. 72 (4), 344–357. https://doi.org/10.31577/GeolCarp.72.4.5.

Krishnamurti, D., 1958. The Raman spectrum of quartz and its interpretation. Proc. Indian Acad. Sci. 47, 276–291.

Lafuente, B., Downs, R.T., Yang, H., Stone, N., 2015. The power of databases: The RRUFF project. In: Armbruster, T., Danisi, R.M. (Eds.), Highlights in Mineralogical Crystallography. Berlin, Germany, W. De Gruyter, pp. 1–30.

Lexa, J., Varga, P., Uhlík, P., et al., 2021. Perlite deposits of the Central Slovakia Volcanic Field ( Western Carpathians ): Geology and properties. Geol. Carpath. 72, 253–281. https://doi.org/10.31577/GeolCarp.72.3.5.

Liu, Y., Zhang, Y., Behrens, H., 2005. Solubility of H2O in rhyolitic melts at low pressures and a new empirical model for mixed H2O–CO2 solubility in rhyolitic melts. J. Volcanol. Geotherm. Res. 143 (1–3), 219–235. https://doi.org/10.1016/j.jvolgeores.2004.09.019.

Mandeville, C., Webster, J.D., Rutherford, M.J., Taylor, B.E., Timbal, A., Faure, K., 2002. Determination of molar absorptivities for infrared absorption bands of H2O in andesitic glasses. Am. Mineral. 87, 813–821. https://doi.org/10.2138/am-2002-0702.

Manley, C.R., 1996. Physical volcanology of a voluminous rhyolite lava flow: the Badlands lava, Owyhee Plateau, southwestern Idaho. J. Volcanol. Geotherm. Res. 71, 129–153. https://doi.org/10.1016/0377-0273(95)00066-6.

Manley, C.R., Fink, J.H., 1987. Internal textures of rhyolite flows as revealed by research drilling. Geology. 15, 549–555.

Marshall, C.P., Dufresne, W.J.B., Rufledt, C.J., 2020. Polarized Raman spectra of hematite and assignment of external modes. J. Raman Spectrosc. 51 (9), 1522–1529. https://doi.org/10.1002/jrs.5824.

McKeown, D.A., 2005. Raman spectroscopy and vibrational analyses of albite: from 25°C through the melting temperature. Am. Mineral. 90, 1506–1517. https://doi.org/10.2138/am.2005.1726.

McLean, C.E., Brown, D.J., Rawcliffe, H.J., 2016. Extensive soft-sediment deformation and peperite formation at the base of a rhyolite lava: Owyhee Mountains, SW Idaho, USA. Bull. Volcanol. 78 https://doi.org/10.1007/s00445-016-1035-2.

McMillan, P., Piriou, B., 1982. The structures and vibrational spectra of crystals and glasses in the silica-alumina system. J. Non-Cryst. Solids 53, 279–298.

Molnár, F., Zelenka, T., Mátyás, E., et al., 1999. Epithermal Mineralization of the Tokaj Mtns., Northeast Hungary: Shallow Levels of Low-Sulfidation. In: Molnár, F., Lexa, J., Hedenquist, J. (Eds.), Epithermal Mineralization of the Western Carpathians, Guidebook series. Society Of Economic Geologists, pp. 109–155.

Mukasa-Tebandeke, I.Z., Ssebuwufu, P.J.M., Nyanzi, S.A., et al., 2015. The elemental, mineralogical, IR, DTA and XRD analyses characterized clays and clay minerals of central and Eastern Uganda. Adv. Mater. Phys. Chem. 5 (2), 67–86. https://doi.org/10.4236/ampc.2015.52010.

Pécskay, Z., Lexa, J., Szakács, A., Seghedi, I., Balogh, K., Konečný, V., Zelenka, T., Kovacs, M., Póka, T., Fülöp, A., Márton, E., Panaiotu, C., Cvetković, V., 2006. Geochronology of Neogene–Quaternary magmatism in the Carpathian arc and intra-Carpathian area: a review. Geol. Carp. 57, 511–530.

Pécskay, Z., Molnár, F., 2002. Relationships between volcanism and hidrotermal activity in the Tokaj Mountains, Northeast Hungary. Geol. Carpath. 53, 303–314.

Pécskay, Z., Balogh, K., Székyné, F.V., Gyarmati, P., 1987. A Tokaji-hegység miocén vulkánosságának K/Ar geokronológiája (The K/Ar geochronology of the Miocene volcanism of the Tokaj mountains). Bull. Hung. Geol. Soc. 117, 237–253 in Hungarian.

Polo, L.A., Giordano, D., Janasi, V.A., Guimarães, L.F., 2018. Effusive silicic volcanism in the Paraná Magmatic Province, South Brazil: Physico-chemical conditions of storage and eruption and considerations on the rheological behavior during emplacement. J. Volcanol. Geotherm. Res. 355, 115–135. https://doi.org/10.1016/j.jvolgeores.2017.05.027.

Renac, C., Mexias, A., Louni-Hacini, A., et al., 2014. Rhyolite petrogenesis and meteoric-hydrothermal alteration at the Maghnia volcanic massif, Northwest Algeria. J. Geochem. Explor. 143, 1–18. https://doi.org/10.1016/j.gexplo.2014.01.022.

Riehle, J.R., Miller, T.F., Paquereau-Lebti, P., 2010. Compaction profiles of ash-flow tuffs: Modeling versus reality. J. Volcanol. Geotherm. Res. 195, 106–120. https://doi.org/10.1016/j.jvolgeores.2010.06.012.

Romine, W.L., Whittington, A.G., Nabelek, P.I., Hofmeister, A.M., 2012. Thermal diffusivity of rhyolitic glasses and melts: effects of temperature, crystals and dissolved water. Bull. Volcanol. 74, 2273–2287. https://doi.org/10.1007/s00445-012-0661-6.

Rowe, M.C., Ellis, B.S., Lindeberg, A., 2012. Quantifying crystallization and devitrification of rhyolites by means of X-ray diffraction and electron microprobe analysis. Am. Mineral. 97, 1685–1699. https://doi.org/10.2138/am.2012.4006.

Rózsa, P., Szöőr, G., Elekes, Z., et al., 2006. Comparative geochemical studies of obsidian samples from various localities. Acta Geol. Hung. 49, 73–87. https://doi.org/10.1556/AGeol.49.2006.1.5.

Ryan, A.G., Russell, J.K., Nichols, A.R.L., Hess, K.-U., Porritt, L.A., 2015. Experiments and models on H2O retrograde solubility in volcanic systems Am. Mineral 100, 774–786. https://doi.org/10.2138/am-2015-5030.

Ryan, A.G., Friedlander, E.A., Russell, J.K., et al., 2018. Hot pressing in conduit faults during lava dome extrusion: Insights from Mount St. Helens 2004–2008. Earth Planet. Sci. Lett. 482, 171–180. https://doi.org/10.1016/j.epsl.2017.11.010.

Ryan, A.G., Russell, J.K., Heap, M.J., et al., 2020. Timescales of porosity and permeability loss by solid-state sintering. Earth Planet. Sci. Lett. 549, 116533 https://doi.org/10.1016/j.epsl.2020.116533.

Scarani, A., Vona, A., Di Genova, D., Al-Mukadam, R., Romano, C., Deubener, J., 2022. Determination of cooling rates of glasses over four orders of magnitude. Contrib. Mineral. Petrol. 177 (3), 35. https://doi.org/10.1007/s00410-022-01899-5.

Scarani, A., Faranda, C.F., Vona, A., Speranza, F., Giordano, G., Rotolo, S.G., Romano, C., 2023. Timescale of Emplacement and Rheomorphism of the Green Tuff Ignimbrite (Pantelleria, Italy). J. Geophys. Res. Solid Earth 128. https://doi.org/10.1029/2022JB026257.

Schipper, C.I., Rickard, W.D.A., Reddy, S.M., et al., 2020. Volcanic $SiO_2$-cristobalite: A natural product of chemical vapor deposition. Am. Mineral. 105, 510–524. https://doi.org/10.2138/am-2020-7236.

Seaman, S.J., Dyar, M.D., Marinkovic, N., 2009. The effects of heterogeneity in magma water concentration on the development of flow banding and spherulites in rhyolitic lava. J. Volcanol. Geotherm. Res. 183, 157–169. https://doi.org/10.1016/j.jvolgeores.2009.03.001.

Seghedi, I., Downes, H., Vaselli, O., Szakaacs, A., Balogh, K., Pécskay, Z., 2004. Post-collisional Tertiary–Quaternary mafic alkalic magmatism in the CarpathianPannonian region: a review. Tectonophysics 393, 43–62. https://doi.org/10.1016/j.tecto.2004.07.05.

Self, S., Randolph-Flagg, N., Bailey, J.E., Manga, M., 2022. Exposed columns in the Valles Caldera ignimbrites as records of hydrothermal cooling, Jemez Mountains, New Mexico, USA. J. Volcanol. Geotherm. Res. 426 https://doi.org/10.1016/j.jvolgeores.2022.107536.

Seligman, A.N., Bindeman, I.N., Watkins, J.M., Ross, A.M., 2016. Water in volcanic glass : from volcanic degassing to secondary hydration. Geochim. Cosmochim. Acta 191, 216–238. https://doi.org/10.1016/j.gca.2016.07.010.

Shields, J.K., Mader, H.M., Caricchi, L., Tuffen, H., Pistone, M., Baumgartner, L., 2016. Unravelling textural heterogeneity in obsidian: Shear-induced outgassing in the Rocche Rosse flow. J. Volcanol. Geoth. Res. 310, 137–158. https://doi.org/10.1016/j.jvolgeores.2015.12.003.

Smith, J.V., 1996. Ductile-brittle transition structures iil the basal shear zone of a rhyolite lava flow, eastern Australia. J. Volcanol. Geotherm. Res. 72, 217–223. https://doi.org/10.1016/0377-0273(96)00009-1.

Stevenson, R.J., Briggs, R.M., Hodder, A.P.W., 1994. Physical volcanology and emplacement history of the Ben Lomond rhyolite lava flow, Taupo Volcanic Centre, New Zealand. New Zeal. J. Geol. Geop. 37, 345–358.

Stolper, E., 1982. Water in silicate glasses: an infrared spectroscopic study. Contrib. Mineral. Petrol. 81, 1–17. https://doi.org/10.1007/BF00371154.

Streck, M.J., Grunder, A.L., 1995. Crystallization and welding variations in a widespread ignimbrite sheet; the Rattlesnake Tuff, eastern Oregon, USA. Bull Volcanol 57 (3), 151–169. https://doi.org/10.1007/BF00265035.

Sweetkind, D.S., Bova, S.C., 2015. Field-Based Description of Rhyolite Lava Flows of the Calico Hills Formation, Nevada National Security Site. Nevada. Sci. Investig. Rep, p. 46.

Szabó, J., 1867. A Tokaj-Hegyalja obsidiánjai (Obsidians of the Tokaj mts) A Magyarhoni Földtani Társulat. Munkálatai 3, 147–172.

Szepesi, J., 2007. Textural zonation and geochemistry of an acidic lava flow base, a case study of Sátor-Krakó range, Abaújszántó, Tokaj-mountains. Acta Geogr. AC Geol. Meteo 2, 105–115.

Szepesi, J., Papp, I., Kovács-Pálffy, P., Gönczy, S., Harangi, S., 2015. Variations in silicic lava hydration, thermogravimetric evidences of volcanogenic processes in lava dome extrusions ACTA GGM Debrec, 10, pp. 57–73.

Szepesi, J., Lukács, R., Biró, T., et al., 2018. Geology of Tokaj mountains obsidians. Archeometriai Műhely 15 (3), 167–179.

Szepesi, J., Lukács, R., Soós, I., et al., 2019. Telkibánya lava domes: Lithofacies architecture of a Miocene rhyolite field (Tokaj Mountains, Carpathian-Pannonian region, Hungary). J. Volcanol. Geotherm. Res. 385, 179–197. https://doi.org/10.1016/j.jvolgeores.2019.07.002.

Tareen, J.A.K., Krishnamurthy, K.V., 1981. Hydrothermal stability of hematite and magnetite. Bull. Mater. Sci. 3, 9–13. https://doi.org/10.1007/BF02748829.

Townson, R., 1797. Travels in Hungary with a Short Account of Vienna in the Year 1793. London XI, pp. 261–303.

Varga, P., Uhlík, P., Lexa, J., et al., 2019. The influence of porosity on the release of water from perlite glass by thermal treatment. Monatsh. Chem. 150, 1025–1040. https://doi.org/10.1007/s00706-019-02410-w.

Vasseur, J., Wadsworth, F.B., Lavallée, Y., et al., 2013. Volcanic sintering: Timescales of viscous densification and strength recovery. Geophys. Res. Lett. 40, 5658–5664. https://doi.org/10.1002/2013GL058105.

Vidal-Solano, J., Demant, A., Paz Moreno, F.A., et al., 2008. Insights into the tectonomagmatic evolution of NW Mexico: Geochronology and geochemistry of the Miocene volcanic rocks from the Pinacate area, Sonora. Bull. Geol. Soc. Am. 120, 691–708. https://doi.org/10.1130/B26053.1.

Wadsworth, F.B., Vasseur, J., Scheu, B., et al., 2016. Universal scaling of fluid permeability during volcanic welding and sediment diagenesis. Geology 44, 19–222. https://doi.org/10.1130/G37559.1.

Watkins, J., Manga, M., Huber, C., Martin, M., 2009. Diffusion-controlled spherulite growth in obsidian inferred from H2O concentration profiles. Contrib. Mineral. Petrol. 157, 163–172. https://doi.org/10.1007/s00410-008-0327-8.

Williams, D.A., Kadel, S.D., Greeley, R., et al., 2004. Erosion by flowing lava: geochemical evidence in the Cave Basalt, pp. 168–181. https://doi.org/10.1007/s00445-003-0301-2.

Wohletz, K.H., 1999. Heat3D. Los Alamos National Laboratory computer code LA-CC 99–27. Los Alamos, New Mexico. https://www.lanl.gov/orgs/ees/geodynamics/Wohletz/KWare/Index.htm.

Wohletz, K., Civetta, L., Orsi, G., 1999. Thermal evolution of the Phlegraean magmatic system. J. Volcanol. Geotherm. Res. 91, 381–414. https://doi.org/10.1016/S0377-0273(99)00048-7.

Zelenka, T., 1964. A Szerencsi-öböl tufaszintjei és fáciesei (Tuff horizons and lithofacies zonation of Szerencs embayment). Bull. Hung. Geol. Soc. 94, 33–52.

Zelenka, T., Gyarmati, P., Kiss, J., 2012. Paleovolcanic reconstruction in the Tokaj Mountains. Cent. Eur. Geol. 55, 49–84. https://doi.org/10.1556/CEuGeol.55.2012.1.4.